This manuscript is a preprint submitted to EarthArXiv and has not been peer reviewed.

Graphical Abstract

Spectrally structured CNN encoding for interpretable and edge-ready fractional vegetation cover mapping using UAS multispectral and imaging spectroscopy

Laura N. Sotomayor, Arko Lucieer, Ryan Haynes, Darren Turner, Johan Barthelemy, Teja Kattenborn

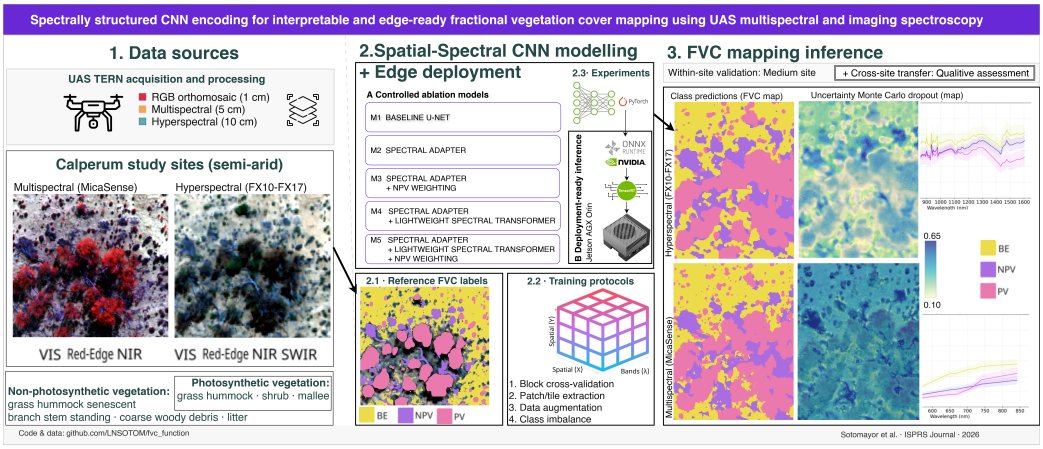

Spectrally structured CNN encoding for interpretable and edge-ready fractional vegetation cover mapping using UAS multispectral and imaging spectroscopy

Laura N. Sotomayor[a], Arko Lucieer[a], Ryan Haynes[a], Darren Turner[a], Johan Barthelemy[b,c], Teja Kattenborn[d]

[a]*School of Geography, Planning, and Spatial Sciences, Hobart, Tasmania, Australia*
[b]*Securing Antarctica's Environmental Future (SAEF), University of Wollongong, Wollongong, , NSW, Australia*
[c]*NVIDIA NVAITC, Australia*
[d]*Sensor-based Geoinformatics (geosense), University of Freiburg, Freiburg, Breisgau, Germany*

Abstract

Fractional vegetation cover (FVC) is a key indicator of semi-arid ecosystem condition, but non-photosynthetic vegetation (NPV) remains difficult to map because dry or senescent vegetation, litter, woody debris, and standing dead material can overlap spectrally with photosynthetic vegetation (PV) and bare ground (BE), especially where shadows, exposed bare earth surfaces, and mixed vegetation–soil pixels occur.

We developed an NPV-aware, spectrally structured convolutional neural network workflow for UAS-based FVC mapping using multispectral and imaging spectroscopy data. The framework used a U-Net backbone with band-aware spectral encoding, lightweight cross-channel attention, NPV-weighted optimisation, data augmentation, spectral characterisation, Monte Carlo dropout uncertainty mapping, cross-site inference, and TensorRT benchmarking.

Ablation experiments showed that NPV-weighted variants produced the largest target-class gains. M5 achieved the highest aggregate NPV F1-score (0.496; +0.148 relative to baseline M1), while M3 achieved the highest mean F1-score (0.745) and mIoU (0.629). The selected MICA 304 px M5 configuration produced stronger segmentation scores (NPV F1 = 0.725; mean F1 = 0.886), whereas the selected FX10–FX17 152 px M5 configuration provided broader VNIR–SWIR information for interpreting NPV, vegetation–

substrate mixtures, dry material, and moisture-sensitive variation. These results indicate a spatial–spectral trade-off: finer spatial resolution improved segmentation detail, while broader spectral information strengthened interpretation of class ambiguity.

Reflectance separability, spectral-index maps, model-derived spectral importance, and uncertainty outputs showed that NPV remained the most uncertain class. Cross-site inference provided qualitative transfer diagnostics, and TensorRT results on Jetson AGX Orin demonstrated compatibility with embedded GPU inference. The workflow provides an interpretable, edge-compatible baseline for sensor-informed FVC mapping.

Keywords: UAS hyperspectral, multispectral imagery, transfer, deep learning, vegetation function mapping, edge deployment

---

1. Introduction

Fractional vegetation cover (FVC) is a key descriptor of ecosystem condition in dryland and semi-arid environments, where sparse herbaceous and woody vegetation, dry plant material, and exposed substrates vary strongly across space and time. In component-based fractional cover products, the land surface is commonly partitioned into photosynthetic vegetation (PV; green vegetation with high chlorophyll content), non-photosynthetic vegetation (NPV; woody material, litter, and dry or senescent plant material), and bare ground (BE; soil, gravel, and rock). These fractions provide an ecologically meaningful representation of active vegetation, dry biomass, and exposed ground, supporting assessments of vegetation condition, degradation risk, productivity, surface stability, grazing capacity, carbon-related ecosystem processes, and ecosystem resilience (Fisk et al., 2019a; Morgan et al., 2020; Melville et al., 2019a; Harrison et al., 2021; Li et al., 2023). In drought-affected drylands, changes in PV, NPV, and BE are particularly important because they can indicate shifts in vegetation dynamics, dry biomass accumulation, soil exposure, and ecosystem function (Brodribb et al., 2020, 2021; Dou et al., 2025).

Optical remote sensing provides a practical basis for estimating these FVC components because PV, NPV, and BE differ in their reflectance across visible (VIS), red-edge, near-infrared (NIR), and shortwave-infrared (SWIR) wavelengths. VIS wavelengths are sensitive to pigment absorption, the red-edge region captures the transition from chlorophyll absorption to enhanced

NIR reflectance, NIR wavelengths are strongly influenced by leaf and canopy structure, and SWIR wavelengths provide complementary sensitivity to water status and dry-matter components (Lewis et al., 2001; Homolová et al., 2013). However, the measured reflectance signal is not uniquely controlled by a single vegetation property, because absorption, scattering, canopy structure, substrate background, illumination, and viewing geometry interact (Kattenborn et al., 2019c,b; Homolová et al., 2013; Wang et al., 2019b; Kattenborn et al., 2024). Vegetation indices (VIs) have therefore been widely used as empirical proxies for greenness, productivity, pigment status, water status, and related ecosystem properties (Tucker, 1979; Merton, 1998; Xue and Su, 2017; Montero et al., 2023; Haynes et al., 2026). In drylands, however, VI interpretation remains context-dependent because dry vegetation, exposed substrate, shadows, canopy structure, and mixed vegetation-soil backgrounds can produce overlapping spectral responses (Lewis et al., 2001; Fisk et al., 2019a; Melville et al., 2019a; Li et al., 2023; Kattenborn et al., 2024). Explicit PV-NPV-BE mapping is therefore important for distinguishing green vegetation, non-photosynthetic dry biomass, and exposed ground, improving the physical interpretability of FVC estimates beyond greenness-based proxies.

Building on these spectral principles, satellite Earth observation data, including multispectral missions such as Landsat and Sentinel-2 and spaceborne imaging spectroscopy missions such as the German Environmental Mapping and Analysis Program (EnMAP), enable repeated and spatially extensive monitoring of vegetation cover across dryland landscapes (Guanter et al., 2015; Fisk et al., 2019b; Storch et al., 2023; Chabrillat et al., 2024; Reddig et al., 2025). Recent EnMAP-based studies have shown that hyperspectral linear unmixing can retrieve subpixel fractional abundances in sparse, low-signal vegetation, although robust validation still requires high-resolution reference data such as UAS imagery (Reddig et al., 2025). Nevertheless, the moderate spatial resolution of many satellite sensors can limit the detection of small vegetation patches, exposed soil, litter, shadows, and fine-scale mixtures of PV, NPV, and BE in heterogeneous rangelands, thereby constraining detailed mapping of local surface composition (Fisk et al., 2019a; Melville et al., 2019a; Morgan et al., 2020; Li et al., 2023).

Imagery from unoccupied aerial systems (UAS) complements satellite-based monitoring by providing centimetre-scale spatial resolution and detailed information on local vegetation structure, canopy gaps, shadows, and exposed ground patterns (Lucieer et al., 2014; Melville et al., 2019b; Turner et al., 2024; Sotomayor et al., 2025a, 2026; Mosig et al., 2026). Integrat-

ing UAS-derived RGB imagery with multispectral data has been shown to improve FVC mapping by capturing fine-scale spatial and spectral variation in PV, NPV, shadows, and exposed BE within semi-arid ecosystems (Bian et al., 2016; Chen et al., 2016; Choi et al., 2016; Melville et al., 2019b; Sotomayor et al., 2025a). UAS multispectral sensors typically acquire data in the VIS, red-edge, and NIR regions, providing sensitivity to greenness, canopy structure, and broad vegetation-soil contrasts (Melville et al., 2019a; Bollard et al., 2022; Sotomayor et al., 2025a). However, although multispectral imagery has demonstrated strength in discriminating and mapping broad biophysical vegetation variables such as leaf area index, and canopy cover, and in monitoring vegetation condition such as greenness, resolving compositional variation among PV, NPV, and BE remains difficult. This limitation arises because broad spectral bands may not capture diagnostic variation associated with pigment degradation, vegetation drying, dry plant material, shadow effects, and heterogeneous soil backgrounds, leading to potential confusion among FVC components (Lewis et al., 2001).

UAS imaging spectroscopy, hereafter referred to as hyperspectral imagery, addresses this spectral limitation by measuring narrow and contiguous bands across the VNIR–SWIR region (Asner and Martin, 2009; Ustin and Gamon, 2010; Zhao et al., 2021). Compared with broadband multispectral imagery, hyperspectral data preserve wavelength-dependent information and provide greater sensitivity to subtle functional differences associated with pigment-related responses, red-edge behaviour, moisture condition, dry vegetation material, canopy structure, and background effects in sparse vegetation communities (Malenovský et al., 2017; Yang et al., 2021; Turner et al., 2023; Wang et al., 2019a; Cotrozzi, 2022; Jutras-Perreault et al., 2023; Cimoli et al., 2024; Haynes et al., 2024). Because the available SWIR range in this study extends only to approximately 1600 nm and does not capture longer SWIR absorption features, moisture-sensitive contrast, dry-material signals, and soil-background interactions are interpreted as trait-sensitive spectral indicators or functional-condition proxies rather than direct biochemical or physiological measurements.

The high dimensionality of UAS hyperspectral imagery creates both an opportunity and a modelling challenge. Dimensionality-reduction and feature-selection approaches, including spectral indices, principal component analysis, spectral summary statistics, and selected narrow bands, are commonly used to simplify hyperspectral inputs and reduce computational burden (Sothe et al., 2020; Cimoli et al., 2020; Kattenborn et al., 2021; Sandino et al., 2025).

These approaches can retain dominant spectral variance or target diagnostic wavelength regions linked to biochemical, structural, and moisture-related vegetation properties, and have been effective for arid vegetation discrimination, vegetation-health assessment, water-content estimation, pigment-proxy mapping, and stress detection (Lewis et al., 2001; Malenovský et al., 2015, 2017; Turner et al., 2023; Montes-Herrera et al., 2024; Sandino et al., 2025; Cimoli et al., 2026; Haynes et al., 2026). However, reducing hyperspectral data to indices, principal components, summary statistics, or a limited set of selected bands may discard wavelength-specific and spectral-shape information needed to separate PV, NPV, BE, and transitional vegetation states. This is particularly problematic where pigment decline, vegetation drying, dry plant material, shadow, and soil-background effects produce overlapping spectral responses (Sothe et al., 2020; Kattenborn et al., 2021). Conversely, retaining full spectral resolution alone does not resolve spatially mixed pixels, diffuse class boundaries, limited training data, or spectral shifts between sites.

Deep learning segmentation algorithms provide a pathway for integrating spectral and spatial information from high-resolution UAS imagery. Convolutional neural networks (CNNs), in particular, have been widely applied in vegetation mapping because they can learn local spatial features such as edges, textures, patch boundaries, and neighbourhood context (Kattenborn et al., 2019a, 2020, 2021; Schiefer et al., 2023; Sotomayor et al., 2025a; Möhring et al., 2025). These features are important for FVC mapping because PV, NPV, BE, and shadows often vary over short distances in response to vegetation structure, senescence, substrate exposure, and local microtopographic conditions. However, in many two-dimensional (2D) CNN applications to hyperspectral imagery, spectral bands are treated as input channels. This allows spectral information to be learned implicitly, but does not explicitly encode wavelength order, band adjacency, or physically meaningful spectral intervals. As a result, the contribution of red-edge regions, SWIR-sensitive wavelengths, or diagnostically important spectral intervals to class predictions may be difficult to control or interpret. Although CNNs have been adapted to learn informative relationships from canopy spectra for plant-trait retrieval (Cherif et al., 2023), spatially explicit segmentation of hyperspectral imagery can benefit from spectral or band-aware encoding that is integrated with CNN-based spatial feature extraction.

The need to jointly represent spectral structure and spatial context has motivated the adaptation of modern vision architectures for remote sensing

segmentation. Transformer-based encoders, including Vision Transformers (ViTs), CNN–Transformer hybrids, and SegFormer-style models (Xie et al., 2021), can capture longer-range spatial dependencies and contextual relationships beyond the local receptive fields of conventional CNNs (Jiang et al., 2023; Joshi and Witharana, 2025; Möhring et al., 2025). In high-resolution vegetation mapping, SegFormer-style architectures have been used for tree-cover delineation and vegetation-condition segmentation from RGB UAS imagery (Veitch-Michaelis et al., 2024; Möhring et al., 2025). Nevertheless, adapting these models to multispectral or hyperspectral imagery remains non-trivial because standard pretrained SegFormer models are typically configured for three-channel RGB inputs. Although transfer learning from pretrained RGB models can reduce annotation requirements and improve model generalisation, extending RGB-pretrained architectures to additional spectral bands requires modification of the initial patch-embedding layer, which can limit the direct reuse of pretrained RGB weights (Xie et al., 2021; Kattenborn et al., 2021; Růžička and Markham, 2024; Chowdhury et al., 2026). Recent hyperspectral ViT adaptations, including HyperSegFormer, address this limitation by modifying Transformer-based segmentation models to process high-dimensional hyperspectral data cubes more directly (Růžička and Markham, 2024). However, Transformer-based models often require larger annotated datasets and greater computational resources when trained directly, which can limit their operational use in ecological applications where labelled data are sparse (Li et al., 2024; Chowdhury et al., 2026).

These data and computational constraints are particularly relevant for UAS vegetation mapping. Prior reviews of CNN-based vegetation studies report a median of approximately 2795 reference observations across UAS- or airborne-based studies in the reviewed literature (Kattenborn et al., 2019a, 2021). Reported reference data volumes vary among sensing platforms, reflecting differences in spatial extent, opportunities for reference-data reuse, and the class separability enabled by finer spatial or structural detail in higher-resolution observations. In this data-constrained context, U-Net encoder–decoder CNNs remain a practical option for UAS-based FVC segmentation because they provide efficient pixel-wise prediction, integrate multiscale spatial context, and can be trained with comparatively modest annotation effort (Huang et al., 2018; Brodrick et al., 2019; Kattenborn et al., 2019a, 2021).

For UAS hyperspectral FVC mapping, the central challenge is therefore not simply to adopt increasingly complex vision architectures, but to preserve

diagnostically relevant spectral information while maintaining the spatial precision, annotation efficiency, and transferability required for component-level segmentation. This is important because transferable UAS-derived FVC products can provide fine-scale reference information for evaluating regional satellite-derived vegetation cover estimates, where coarser pixels often integrate multiple ground-cover components. New site inference remains difficult because vegetation condition, senescence, soil background, illumination, shadow, and substrate exposure can shift spectral distributions between training, validation, and deployment areas. Hyperspectral workflows also involve trade-offs among spectral richness, spatial resolution, signal-to-noise ratio, storage requirements, calibration complexity, and computational cost (Kattenborn et al., 2021; Chowdhury et al., 2026). Spectral adapter modules provide one mechanism for addressing these constraints by translating high-dimensional hyperspectral inputs into structured spectral representations before spatial decoding, allowing CNN-based models to exploit spectral information while retaining local boundary-delineation ability (Braham et al., 2025). In this study, spectral structure refers to the explicit modelling of relationships among ordered spectral bands, rather than relying solely on channel mixing that does not encode wavelength order.

Building on existing UAS-derived FVC labels (Sotomayor et al., 2025b) and prior CNN-based FVC segmentation work in sparse rangelands (Sotomayor et al., 2025a), this study extends UAS-based FVC mapping to imaging spectroscopy by evaluating whether spectrally structured CNN variants can improve class separability while retaining efficient spatial segmentation. Related work has demonstrated the reuse of UAS-derived 2D labels for scalable 2D–3D transfer and growth-form benchmarking in rangeland ecosystems (Sotomayor et al., 2026); here, the focus remains on 2D hyperspectral FVC mapping and new-site inference.

Operational feasibility is also important for UAS-based environmental monitoring because large hyperspectral rasters, high spectral dimensionality, and tiled inference can make deployment workflows computationally demanding. Although high-performance computing is suitable for model training and large-scale experimentation, field deployment in remote or connectivity-limited environments requires lightweight inference workflows that can operate near the sensor on portable, power-constrained GPU platforms. Edge computing can reduce acquisition-to-processing latency, limit the transfer of full-resolution hyperspectral data to cloud or HPC infrastructure, and lower energy demand, supporting more sustainable and cost-effective operation for

battery limited UAS missions (Koubaa et al., 2023; Liu et al., 2021; López-Fandiño et al., 2024). Recent work has therefore emphasised onboard and edge AI for drone remote sensing (Koubaa et al., 2023), optimised deep learning on edge computer such as the NVIDIA Jetson platforms (Mittal, 2019), Jetson AGX Orin benchmarking for high-resolution multispectral anomaly detection (López-Fandiño et al., 2024), and low-compute hyperspectral models for onboard remote-sensing applications (Haut et al., 2019; Růžička and Markham, 2024).

Accordingly, this study makes three primary contributions:

1. We adapt and extend a previously developed CNN-based FVC segmentation framework (Sotomayor et al., 2025a) for multi-sensor UAS optical imagery, with emphasis on the spectrally ambiguous NPV component. The upgraded framework evaluates band-aware spectral encoding through controlled ablation experiments comparing a baseline U-Net, a spectral-adapter CNN, and a spectral-adapter CNN with a lightweight spectral transformer, while separately assessing NPV-weighted optimisation for FVC class imbalance.

2. We assess post-inference spectral characterisation and model interpretability by relating predicted BE, NPV, and PV classes to reflectance responses, pairwise spectral separability, post-inference spectral-index maps, Monte Carlo dropout-based uncertainty, and class-wise model-derived spectral importance scores, with particular attention to the spectral ambiguity of NPV.

3. We evaluate edge-deployment feasibility by exporting selected multispectral and imaging spectroscopy models to ONNX, converting them to TensorRT engines, and benchmarking numerical consistency, model footprint, inference latency, throughput, and precision-dependent performance on Jetson AGX Orin hardware.

2. Materials

2.1. Study area and datasets

We tested the spectrally structured CNN at one site (SASMDD0001), known as an AusPlot site that is part of the Australian Terrestrial Ecosystem Research Network (TERN) and inferenced in another TERN Ausplot (SASMDD0013) (White et al., 2012), each representing similar vegetation types as

defined by the National Vegetation Information System (NVIS) (DCCEEW, 2017). The sites sample the predominant structural formations of this semi-arid area, encompassing a range of vegetation types, soil characteristics, and structural complexities (White et al., 2012; TERN, 2026) (detailed in Table 1). The study sites covered a total area of 19 hectares (ha) and are located at Calperum Station near Renmark, South Australia (see Figs. 1 and Fig.2, where further details of UAS imagery processing is described in Section 3.1). This area experiences low annual rainfall (average 265 mm) and an average temperature of 17 °C.

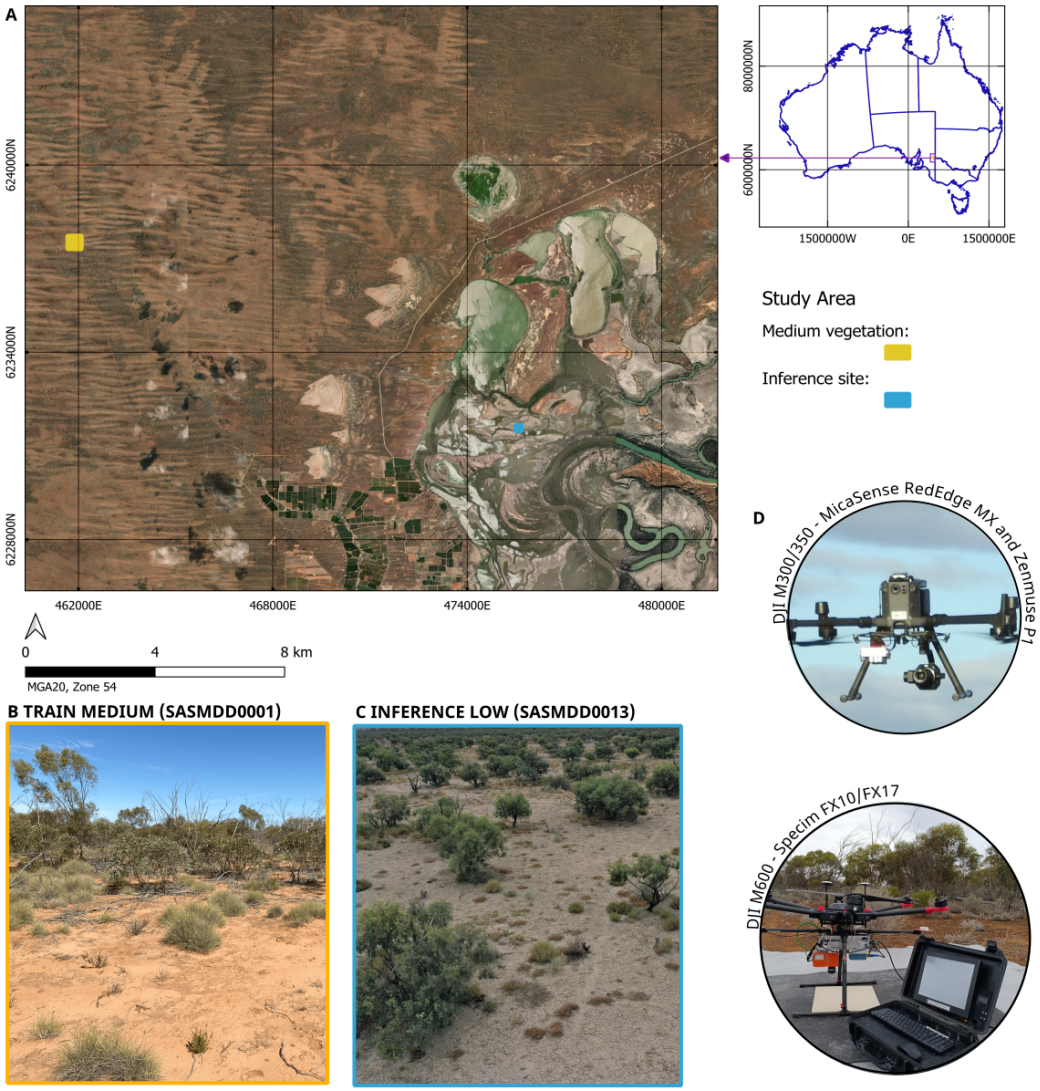

Figure 1: **A** Location of the two study sites (rectangle coloured boxes in map top-left) at Calperum Station, South Australia, each representing a different vegetation community (**B** for medium site trained and **C** for low site used as inference). **D** the UAS platforms used for data acquisition during the survey.

The medium density site (SASMDD0001) sits on a stable longitudinal dunefield and dune crest, and supports a regenerating multi-stemmed mallee canopy dominated by *Eucalyptus socialis* subsp. *socialis*, *E. cyanophylla* and *E. dumosa* (mostly 0.5-5 m), influenced by past fire events, over a sparse un-

derstorey of *Triodia scariosa* hummock grasses (0.01–3.70 m, median 0.30 m) (see Fig. 2B, C). Here, standing and emergent dead branches persisting after fire add to the coarse woody debris and litter, creating structural diversity through mallee stems, *Triodia* hummocks, and NPV branches. On the other hand, the low vegetation site (SASMDD0013) is a low open woodland of *Eucalyptus largiflorens* (0.6–5.0 m, median 2.5 m) on a floodplain, with a sparse ground cover of *Maireana pyramidata* chenopod shrubs (0.2–0.6 m) and scattered annual grasses and forbs (see Fig. 2G, H). The soil surface is cryptogam crusted with poor drainage over a reddish-brown calcareous sandy loam, consistent with a Calcarosol.

Table 1: Site descriptions including area, land system, dominant vegetation, height, structure and growth forms (White et al., 2012; TERN, 2021; TERN et al., 2022; TERN, 2026)

AusPlot IDs	**Site area**	**Land system and soil type**	**Dominant vegetation**	**Height of strata**	**Growth forms and structural components**
SASMDD0001 (medium)	369 m x 400 m (≈ 15 ha)	Stable inland dune-swale system; reddish loamy sand	Low open woodland of multi-stemmed mallee *Eucalyptus* spp. over sparse understorey of *Triodia scariosa* hummock grasses and shrubs	Upper (Mallee trees) and Ground (mainly *Triodia*): 0.5–5 m	Hummock grass, multi-stemmed mallee trees, shrubs, coarse woody debris, and litter. Standing/emergent NPV branches/stem that still stand after regeneration after fire and emergent dead branches
SASMDD0013 (low)	152 m × 186 m (≈ 2.8 ha)	Floodplain plain; soil surface recorded as cryptogam surface with poor drainage; reddish-brown calcareous sandy loam	*Maireana pyramidata* (Black bluebush) low open shrubland with scattered annual grasses and forbs	Tree/shrub layer: 0.6–5.0 m for *Eucalyptus largiflorens* (median 2.5 m); chenopod shrub layer: 0.2–0.6 m for *Maireana pyramidata* (median 0.4 m)	Low open *Eucalyptus largiflorens* woodland with sparse chenopod shrubs, annual grasses, and forbs

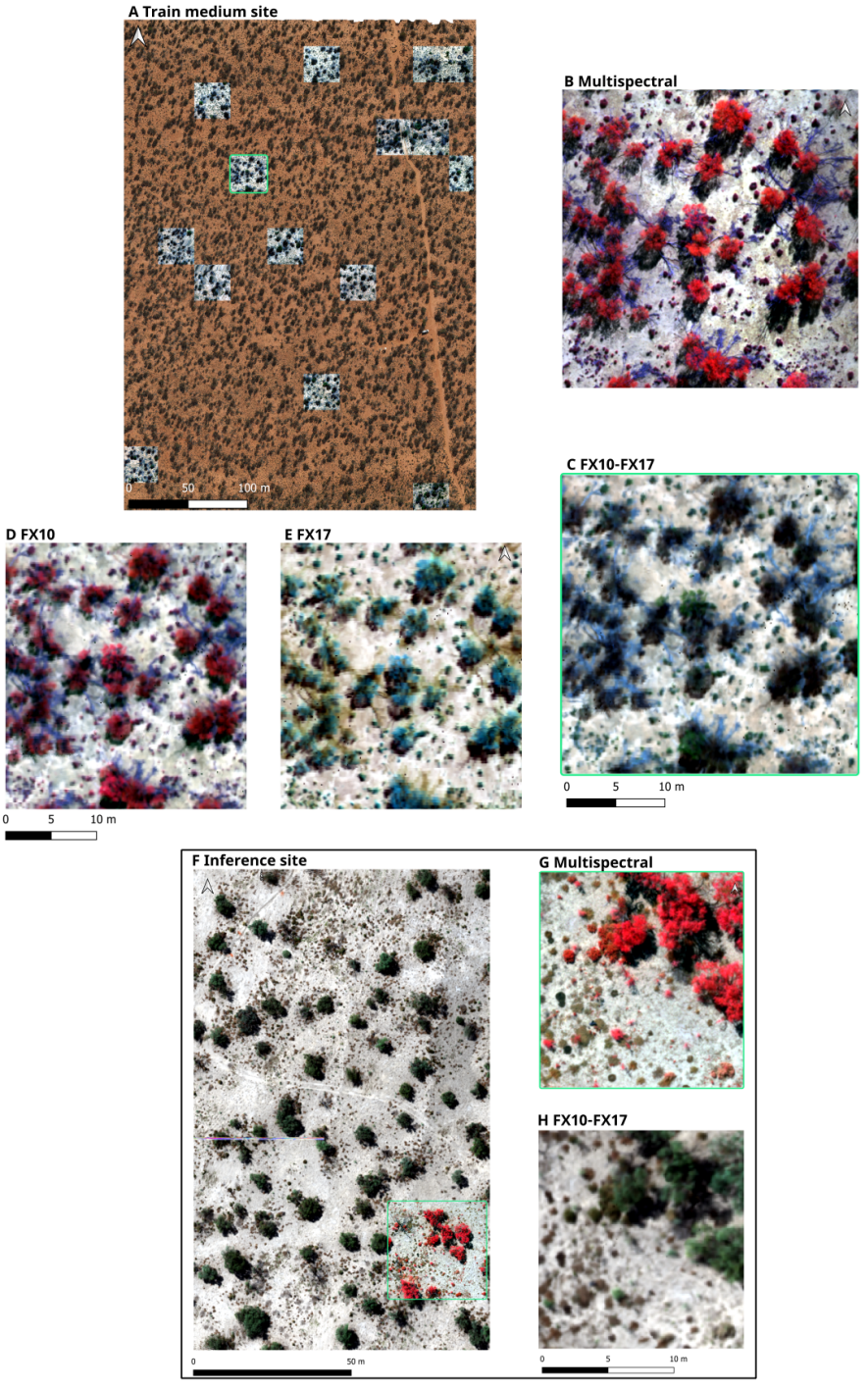

Figure 2: Multi-sensor remote sensing imagery across training and inference sites with contrasting vegetation structure. **A** RGB orthomosaic of the medium vegetation training site, overlaid with 15 labelled hyperspectral tiles (3070 × 3070 pixels); the green box marks the subset shown in **B**–**E**. **B**–**E** Enlargements of this subset: **B** multispectral imagery (NIR-842 nm, Red-668 nm, Blue-475 nm), **C** fused FX10–FX17 imagery (639.585 nm, 551.015 nm, 468.725 nm), **D** FX10 imagery (800.445 nm, 609.955 nm, 529.695 nm), and **E** FX17 imagery (1597.010 nm, 1299.800 nm, 999.630 nm). **F** FX10–FX17 orthomosaic of the low-vegetation inference site, characterised by sparse vegetation and extensive exposed ground; the green box marks the subset shown in **G**–**H**. **G**–**H** Enlargements of this subset from multispectral and fused FX10–FX17 imagery, respectively, using the band combinations in **B** and **C**.

3. Methods

The proposed workflow integrates band-aware CNN-based FVC segmentation, post-inference spectral characterisation, and edge-deployment benchmarking. After the study area and datasets are described in Section 2, Section 3.1 details the generation of calibrated reflectance imagery and FVC reference labels from the multi-sensor UAS optical datasets. The experimental framework compares a baseline CNN with spectral-encoding CNN variants (Section 4). Model outputs are evaluated and interpreted using class probabilities, Monte Carlo dropout-based uncertainty, class-wise reflectance responses, pairwise spectral separability, post-inference spectral-index maps, and model-derived spectral importance scores. Finally, the best-performing models are exported to ONNX, converted to TensorRT, and benchmarked on Jetson hardware to assess the feasibility of scalable band-aware FVC segmentation for edge deployment. The full pipeline, *hyperFVC*, is publicly available at `https://github.com/LNSOTOM/fvc_function`.

3.1. UAS acquisition and processing

3.1.1. UAS platforms and sensors

Datasets were acquired using DJI Matrice RTK UAS platforms equipped with optical imaging sensors. The May 2022 campaign, including the medium density site, was conducted with a DJI Matrice 300 RTK platform carrying a DJI Zenmuse P1 RGB camera and a MicaSense (MICA) RedEdge-MX/Dual multispectral sensor. The low density inference site was acquired in March 2024 using the updated DJI Matrice 350 RTK platform. Multispectral imagery comprised ten broad bands: Blue-444, Blue-475, Green-531, Green-560, Red-650, Red-668, Red Edge-705, Red Edge-717, Red Edge-740, and NIR-842 nm. Flight parameters were optimised for each optical sensor, with RGB and multispectral imagery collected at 80 m above ground level at a flying speed of 8 m/s, resulting in ground sampling distances of approximately 1 cm/pixel and 5 cm/pixel, respectively. Further details on data collection and preprocessing are provided in the TERN drone data collection and imagery processing protocols (TERN, 2022; Montes-Herrera et al., 2025).

The imaging spectroscopy sensors were mounted on a DJI Matrice 600 UAS (DJI, Shenzhen, China). The payload was designed as a modular system, allowing different imaging spectroscopy sensors to be interchanged. In this study, two Specim sensors (Specim, Oulu, Finland) were flown consecutively for each site: the FX10, which measures in the visible to near-infrared

region of the electromagnetic spectrum (400–1000 nm), and the FX17, which measures in the near-infrared to shortwave-infrared region (900–1700 nm). The FX10 and FX17 acquired 224 and 112 spectral bands, respectively, before preprocessing and removal of unusable or overlapping bands. The average Full Width at Half Maximum (FWHM) of the FX10 is 5.5 nm and 8 nm for the FX17. The pose orientation system (POS) for determination of sensor location and orientation was the Advanced Navigation Certus Evo, which was hard-mounted to the sensors with the lever arm offsets measured with millimeter precision. Each sensor was flown in separate flights, one after the other with brief (<15 min) time between flights to swap sensors. Both sensors were flown at 90 m above ground level at a flying speed of 4 m/s resulting in a spatial resolution of approximately 6 cm/pixel for the FX10 and 9.6 cm for the FX17 (before re-sampling both to 10 cm). For more information on the UAS and sensor configuration, see Haynes et al. (2025).

3.1.2. UAS RGB and multispectral processing

The RGB and multispectral imagery were georeferenced using the DJI D-RTK2 base station and the onboard Global Navigation Satellite System Real-Time Kinematic (GNSS RTK) receiver, providing an expected absolute positioning accuracy of approximately 5 cm without the use of ground control points. Imagery was processed in Agisoft Metashape Professional v. 2.0 following the TERN drone RGB and multispectral image processing protocols (TERN, 2021, 2022; TERN et al., 2022). The processing workflow generated spatially co-registered RGB and multispectral orthomosaics for downstream analysis. Multispectral imagery was radiometrically calibrated using a camera calibration panel and co-registered with the RGB product during processing. The calibrated multispectral images were orthorectified using the RGB-derived surface model to produce multispectral orthomosaics spatially aligned with the RGB orthomosaic. Further details of this workflow are provided in (TERN, 2022; Montes-Herrera et al., 2025). Together, these steps produced georeferenced, co-registered RGB and multispectral reflectance products suitable for subsequent model development and analysis.

Multispectral reflectance scaled-integer storage for CNN modelling. The multispectral orthomosaics were stored as scaled integers to reduce file size while preserving reflectance precision. Valid float32 reflectance values were multiplied by a scale factor of 10,000 and converted to int16, preserving four decimal places of precision and maintaining consistency with the hyperspec-

tral integer-scaled data products. Invalid pixels, including NaN and existing nodata values, were excluded from scaling and assigned a nodata value of −1. Valid reflectance values can be recovered by dividing the stored values by 10,000.

3.1.3. UAS Imaging spectroscopy processing

The hyperspectral imagery was radiometrically calibrated, geometrically corrected, and converted to surface reflectance. For radiometric correction and georectification, both sets of imagery (FX10 and FX17) were processed line by line in Caligeo Pro, using factory calibration files provided by Specim and high accuracy post-processed data from the POS. After this processing, the individual passes were trimmed to remove the jagged edges (retaining the central 80 - 90 percent of the imagery). These hyperspectral orthomosaic image strips were then co-registered to the RGB mosaic from 2022 using optical flow method eFOLKI (Iteration: 8., radius: [16. 8. 4]., rank: 4., levels: 6) to ensure pixel-level alignment. Finally, the spatially aligned image strips were converted to reflectance using Atmospheric Radiative Transfer Modelling (ARTM) software DROACOR (RESE, 2025). Noise-dominated and water absorption bands were interpolated prior to analysis. Specifically, the bands associated with the absorption feature at 1400 nm were interpolated (between wavelengths 1320.9 and 1419.62 nm). To reduce high frequency noise while preserving the diagnostic absorption features, the reflectance for each pass were minimally smoothed using a Savitsky-Golay (SAVGOL) filter (window length 3, poly order 1). Then, all passes were mosaicked in ENVI using the seamless mosaic tool. Further details on imaging spectroscopy data preprocessing can be found (Haynes et al., 2025, 2026).

FX10–FX17 spectral trimming and stacking for CNN modelling. For CNN modelling, the FX10 and FX17 hyperspectral orthomosaics were spectrally trimmed and concatenated to produce a single VNIR–SWIR reflectance stack. The original FX10 and FX17 products contained 224 and 112 bands, covering 397.765–1003.915 nm and 933.330–1719.595 nm, respectively (Table 2). Trimming was performed to remove noise-dominated sensor-edge channels and minimise redundant spectral overlap between the two sensors. The ENVI metadata were also inspected for bands flagged as interpolated, where reflectance values are estimated from neighbouring spectral channels during sensor calibration rather than measured as fully independent observations. This information was considered when defining the retained wave-

length ranges.

For the FX10 sensor, bands 10–215 were retained, yielding 206 bands from 421.345 to 978.565 nm. Bands 1–9, corresponding to 397.765–418.725 nm, were removed because they occur at the lower edge of the FX10 spectrum, where calibration uncertainty and reduced signal-to-noise ratio may affect reflectance stability. Bands 216–224, corresponding to 981.375–1003.915 nm, were also removed to avoid redundancy with the beginning of the FX17 spectral range.

For the FX17 sensor, bands 7–96 were retained, yielding 90 bands from 978.850 to 1604.130 nm. Bands 1–6 were omitted because they overlapped with the retained FX10 range, with FX17 band 7 beginning at 978.850 nm, close to the final retained FX10 band at 978.565 nm. Bands 97–112 were excluded from the upper SWIR edge, where reflectance estimates are more susceptible to noise and calibration uncertainty. The final combined FX10–FX17 stack therefore contained 296 bands, with FX10 bands 10–215 followed by FX17 bands 7–96, covering an overall wavelength range of 421.345–1604.130 nm.

Before stacking, spatial consistency between the trimmed FX10 and FX17 orthomosaics was checked using projection, geotransform, and raster dimensions. Where grid differences were present, the FX17 orthomosaic was aligned to the FX10 grid using an in-memory GDAL VRT warp, with the FX10 extent, pixel dimensions, and projection used as the spatial reference. The FX10 orthomosaic itself was not resampled. Bilinear resampling was applied to the FX17 reflectance data because they represent continuous values, whereas nearest-neighbour resampling was reserved for categorical rasters such as masks or class labels. The final stack was written as an ENVI raster using band-sequential interleaving. No spectral resampling to a common wavelength grid was applied; instead, the retained sensor-specific bands were concatenated along the band dimension at their native wavelength sampling.

Table 2: Spectral configuration of the FX10, FX17, and combined FX10–FX17 hyperspectral datasets.

Dataset	Band range	Number of bands	Wavelength range (nm)
FX10 full range	1–224	224	397.765–1003.915
FX17 full range	1–112	112	933.330–1719.595
FX10–FX17 used stack	FX10: 10–215; FX17: 7–96	296	421.345–1604.130
FX10 component	10–215	206	421.345–978.565
FX17 component	7–96	90	978.850–1604.130

3.2. 2D reference data extraction for U-Net segmentation models

U-Net-based semantic segmentation requires co-registered predictor rasters and categorical reference masks prepared as paired image–mask tiles. Two-dimensional (2D) predictor–reference datasets were therefore generated for multispectral and hyperspectral model configurations using a common fractional vegetation cover (FVC) class schema: bare ground (BE = 0), non-photosynthetic vegetation (NPV = 1), and photosynthetic vegetation (PV = 2) (see Table 3 and Fig. 3). This schema followed the 2D reference-label framework developed for site-specific FVC mapping by Sotomayor et al. (2025a,c).

3.2.1. Annotation and mask alignment

Reference labelling. We adopted the orthomosaic tiling and reference-data generation workflow described by Sotomayor et al. (2025a). For manual interpretation, 15 multispectral source tiles were randomly selected and converted to 8-bit false-colour composites using the blue, red, and NIR bands. Reference polygons for BE, NPV, and PV were digitised in LabelMe, an open-source annotation platform (Wada and others, 2021), with Efficient-SAM used as an AI-assisted interactive segmentation model to support polygon delineation (Xiong et al., 2023, 2024). The resulting labels were inspected and refined in QGIS 3.28.0-Firenze to correct inaccurate automated delineations and improve class-boundary consistency. The refined polygons were then merged into a unified vector label dataset and rasterised according to the site-specific class characteristics summarised in Table 3 and illustrated in Fig. 5. The medium-density training site used in this study contained the three FVC classes BE, NPV, and PV outlined in Table 3 and and illustrated with examples in Fig. 3.

Sensor-specific mask alignment. The refined annotation masks were first prepared at 1 cm resolution and then downsampled to the 5 cm multispectral grid using majority-vote resampling. Each multispectral predictor tile was used as the reference grid to ensure matching extent, transform, and raster dimensions. For the hyperspectral configurations, the 5 cm multispectral-aligned masks were further downsampled to the 10 cm FX10, FX17, and combined FX10–FX17 grids, again using majority-vote resampling with the corresponding predictor tile as the reference. This produced aligned masks for each sensor configuration while preserving the common BE, NPV, and PV class schema. Invalid or unlabelled pixels were assigned to the ignore class and excluded from the loss during training.

Table 3: FVC class definitions and structural subclasses used for reference-label generation at the medium-density training site. Structural subclasses were used to guide annotation but were aggregated into the three modelled FVC classes: BE, NPV, and PV.

ID	**Class**	**Structural subclass**	**Annotation definition**
0	BE	Bare ground	Exposed bare ground or substrate without visible vegetation cover.
1	NPV	Standing branch/stem	Attached, upright, or emergent dead woody material, including branches or stems persisting after fire and lacking live foliage; often associated with offset shadows.
		Coarse woody debris	Larger detached dead woody material, including fallen branches or stems lying on the ground.
		Litter	Fine dead plant material on the ground, including leaves, bark fragments, and small twigs.
		Senescent hummock grass	Dry or ageing hummock grass with limited or no visible photosynthetic foliage.
2	PV	Mallee	Live multi-stemmed eucalypt growth, typically resprouting from lignotubers or epicormic buds after fire.
		Shrub	Live perennial woody plants with multiple stems; height classes may be recorded separately as < 2 m or ≥ 2 m.
		Hummock grass	Live spiny perennial grass forming rounded hummocks that may expand into open rings with age.

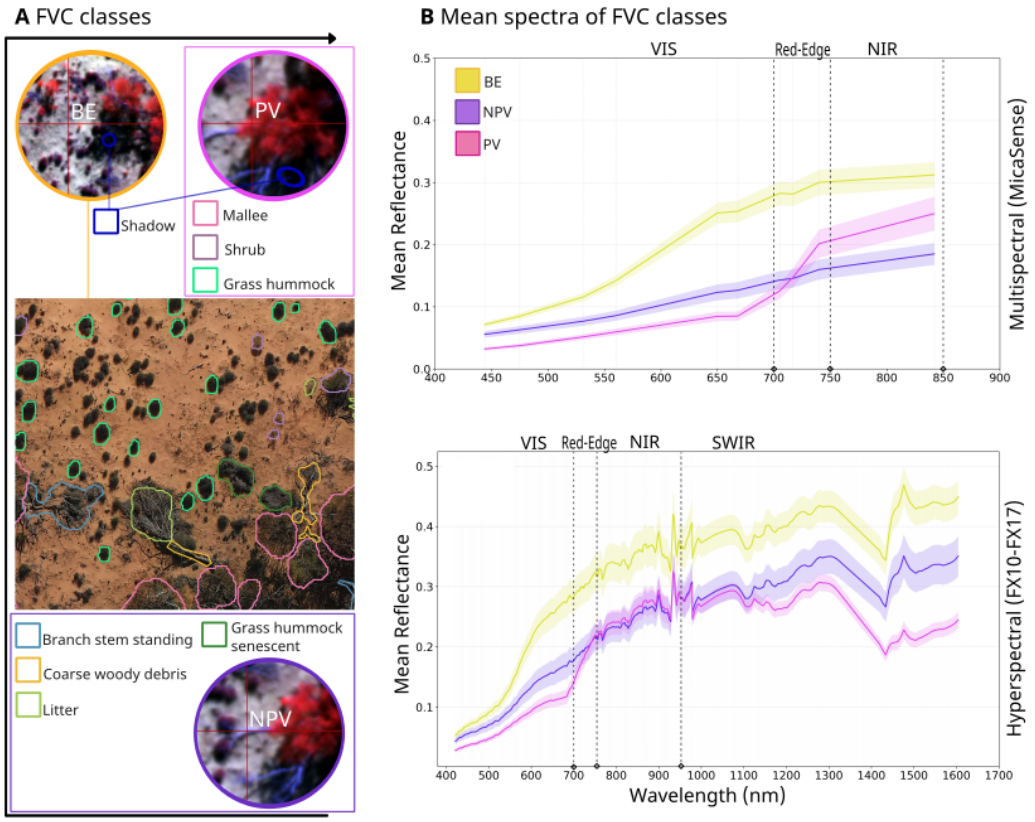

Figure 3: FVC classes and their spectral separability in multispectral and hyperspectral imagery. **A** Enlarged RGB image subset of the study area showing representative structural components used to interpret the three FVC classes: BE, PV, and NPV. PV includes live mallee, shrub, and grass hummock components, whereas NPV includes standing dead stems, coarse woody debris, litter, and senescent hummock grasses. Shadowed pixels are highlighted as an image-level confounding condition that can reduce local reflectance and complicate visual separation among BE, PV, and NPV, but they were not treated as a separate FVC class. These components provide ecological context for the image labels but were aggregated into BE, PV, and NPV for model training and inference. **B** Mean spectral reflectance responses for BE, PV, and NPV, shown as coloured lines with shaded 95% confidence intervals calculated from all reference data tiles at the study site. The top panel shows MicaSense multispectral responses across the VIS, Red-Edge, and NIR regions, while the bottom panel shows FX10–FX17 hyperspectral responses across the VIS, Red-Edge, NIR, and SWIR regions. Vertical dashed lines indicate approximate spectral-region boundaries.

3.2.2. Sensor-specific predictor preparation

Predictor rasters were prepared separately for multispectral and hyperspectral configurations because the sensors differed in spatial resolution, tile size, and spectral dimensionality.

Multispectral predictors. The multispectral orthomosaic was used as the predictor source on a 5 cm raster grid. Source tiles were generated at 614×614 pixels, corresponding to approximately 30.70×30.70 m. Reflectance values followed the project scaled-integer convention, where valid float reflectance values were multiplied by 10,000 and stored as signed 16-bit integers, while invalid or NoData pixels retained the project NoData value.

Hyperspectral predictors. The FX10 and FX17 reflectance mosaics were used as predictor sources on a 10 cm raster grid. Three hyperspectral configurations were prepared: FX10-only, FX17-only, and combined FX10–FX17. Spectral inputs used FX10 bands 10–215 and FX17 bands 7–96; for the combined configuration, the selected bands from both sensors were concatenated along the spectral dimension before patch extraction. Hyperspectral source tiles were generated at 304×304 pixels, corresponding to approximately 30.40×30.40 m.

3.2.3. Scale-specific crop and patch extraction

Patch extraction was performed separately for the multispectral and hyperspectral predictor configurations to preserve each sensor's native spatial resolution while producing U-Net-compatible input sizes (Table 4).

Multispectral configuration. Each 614×614 multispectral predictor–mask tile was centre-cropped to 608×608 pixels by removing three pixels from each edge. No spatial resampling was applied. The 608×608 size was selected because it is divisible by 32, ensuring compatibility with the U-Net encoder–decoder structure. The cropped tiles were then subdivided into 304×304 patches using 50% overlap, corresponding to a stride of 152 pixels and patch start positions of 0, 152, and 304 pixels in both row and column directions. Each multispectral source tile therefore generated nine paired samples.

Hyperspectral configurations. The 304×304 hyperspectral source tiles were not resized or resampled. Instead, input samples were extracted as spatial windows from the original tile extent. For the 304×304 configuration, the full tile was used directly, producing one sample per source tile. For the

224×224 configuration, row and column offsets of 0 and 80 pixels produced a 2×2 layout, yielding four samples per tile with 144 pixels of overlap between adjacent windows. For the 152×152 configuration, offsets of 0, 76, and 152 pixels produced a 3×3 layout, yielding nine samples per tile with 50% overlap. Larger hyperspectral patches increased the spatial context represented by each sample but reduced the number of samples available for training and evaluation.

For all configurations, predictor rasters and reference masks were matched by tile ID and processed using identical crop or window offsets to preserve pixel-wise correspondence between inputs and labels. Patches derived from the same original source tile were kept within the same training, validation, or test subset to avoid spatial leakage between data splits.

Table 4: Predictor–reference patch extraction summary. Patch totals are reported per predictor configuration.

Sensor/profile	Spatial scale	Source tile	Patch size	Patches/tile	Total patches	Train/val/test
Multispectral	5 cm	$614 \times 614 \rightarrow 608 \times 608$	304×304	9	135	72 / 27 / 36
FX10, FX17, FX10–FX17	10 cm	304×304	152×152	9	135	72 / 27 / 36
FX10, FX17, FX10–FX17	10 cm	304×304	224×224	4	60	32 / 12 / 16
FX10, FX17, FX10–FX17	10 cm	304×304	304×304	1	15	8 / 3 / 4

4. Experiments

4.1. Experimental design

FVC mapping was formulated as a dense semantic segmentation task in which each valid pixel was assigned to one of three classes: BE, NPV, or PV. Invalid or unlabelled pixels were assigned an ignore label of (-1) and were excluded from loss computation and metric evaluation.

The experimental design used a modular ablation framework to evaluate how band-aware spectral encoding, lightweight cross-channel attention, and NPV-weighted optimisation affected UAS-based FVC segmentation. All variants used the same U-Net-style spatial encoder–decoder backbone and differed only in the spectral front-end, transformer setting, and class-weighting configuration. This allowed performance differences to be attributed primarily to the architectural and loss-weighting components under evaluation.

Five model variants were compared: a baseline U-Net CNN, a spectral-adapter CNN, an NPV-weighted spectral-adapter CNN, a spectral-adapter

CNN with lightweight spectral transformer, and an NPV-weighted spectral-adapter transformer CNN. Table 5 summarises the ablation sequence. Code-level implementation details are provided in the GitHub repository `https://github.com/LNSOTOM/fvc_function`.

Table 5: Model variants used to evaluate spatial convolutional learning, band-aware spectral-channel embedding, lightweight cross-channel attention, and class-weighted loss optimisation. Class weights are reported in the order BE, NPV, and PV.

Variant	Description	Spectral mode	Transformer	Weighted loss	Isolated comparison
M1	Baseline U-Net CNN	`no_spectral`	0	–	reference spatial encoder–decoder
M2	Spectral-adapter CNN	`enhanced`	0	–	effect of band-aware spectral-channel embedding
M3	Weighted spectral-adapter CNN	`enhanced`	0	$[1, 2, 1]$	effect of NPV up-weighting without transformer
M4	Spectral-adapter CNN with lightweight spectral transformer	`enhanced`	1	–	effect of lightweight cross-channel interaction modelling
M5	Weighted spectral-adapter CNN with lightweight spectral transformer	`enhanced`	1	$[1, 2, 1]$	combined spectral-channel embedding, cross-channel attention, and imbalance-aware optimisation

4.1.1. Baseline U-Net CNN

The baseline model provided the spatial encoder–decoder reference against which all spectrally structured variants were compared (Ronneberger et al., 2015). In this configuration, reflectance bands were passed directly to the shared U-Net backbone described in Section 4.2.2, without the spectral adapter or lightweight spectral transformer. This model quantified the performance achievable when spectral bands were learned implicitly by standard convolutional feature extraction.

4.1.2. Spectral-adapter CNN

The spectral-adapter CNN was implemented as a study-specific combination of established architectural components, rather than as a direct reimplementation of a single published adapter model. The design combined squeeze-and-excitation-style channel recalibration (Hu et al., 2019), hyperspectral spatial–spectral attention concepts (Wang et al., 2019a), pixel-wise (1×1) convolutional projection (Lin et al., 2014), and the shared U-Net segmentation backbone (Ronneberger et al., 2015).

The adapter was inserted before the U-Net encoder to perform band-aware recalibration and spectral-channel embedding. It first estimated band-wise weights from the input reflectance patch and used these weights to modulate the relative contribution of each spectral channel. This provided an adaptive spectral reweighting step before spatial decoding, allowing the model to emphasise channels useful for separating BE, NPV, and PV.

After band recalibration, the adapter projected the input bands into a fixed 32-channel learned spectral embedding using stacked (1×1) convolutional operations with batch normalisation, Gaussian Error Linear Unit (GELU) activation, and dropout (Lin et al., 2014; Hendrycks and Gimpel, 2023). The notation "32 ch" refers to learned spectral feature channels, not to 32 original reflectance bands. For multispectral inputs, this acted as a band-aware remapping module. For hyperspectral inputs, it also provided trainable dimensionality reduction from the larger input band set to the same fixed embedding dimension.

The module did not explicitly use wavelength-centre or bandwidth metadata; therefore, learned weights were spectral-channel specific under a fixed input band order rather than wavelength-parameterised. This variant tested whether explicit spectral-channel encoding improved BE, NPV, and PV segmentation relative to the baseline U-Net CNN.

4.1.3. Spectral-adapter CNN with lightweight spectral transformer

The transformer-enabled variants added a lightweight cross-channel attention block after the spectral adapter and before the U-Net encoder. This block was designed as a computationally efficient channel-attention module rather than as a full vision transformer over spatial image tokens. The design was inspired by transformer self-attention (Vaswani et al., 2023) and hyperspectral transformer studies that use attention to model spectral signatures and joint spectral–spatial representations (He et al., 2021; Hong et al., 2022; Růžička and Markham, 2024; Makarov et al., 2025).

The module operated on the 32-channel learned spectral embedding produced by the adapter. Instead of applying self-attention across all spatial pixels, it summarised the adapted feature tensor using global spatial descriptors and used these descriptors to estimate cross-channel interactions. The resulting attention-weighted representation was passed through a (1×1) projection, residual connection, normalisation, and lightweight feed-forward convolutional block.

This design retained the main purpose of transformer-style spectral interaction modelling while avoiding the memory cost of full spatial self-attention. It is therefore interpreted as lightweight global channel attention over the learned spectral embedding, rather than as a conventional ViT-style token transformer. The corresponding ablation tested whether explicit cross-channel interaction modelling improved FVC segmentation beyond the spectral-adapter CNN alone.

4.1.4. Class-weighted spectral-adapter variants

Class-weighted optimisation was evaluated as a loss-function ablation for the spectral-adapter CNN and the spectral-adapter transformer CNN. These variants used the class-weighting term of focal loss (Lin et al., 2017), with $(\alpha = [1, 2, 1])$ for BE, NPV, and PV, respectively. Thus, NPV pixels contributed more strongly to the loss than BE or PV pixels during training.

The weighting was applied only to M3 and M5. M3 isolated the effect of NPV up-weighting for the spectral-adapter CNN, whereas M5 tested the same weighting in combination with lightweight cross-channel attention. Because the input data, class definitions, backbone structure, and evaluation protocol were otherwise held constant, performance differences between weighted and unweighted variants were interpreted as the effect of imbalance-aware optimisation.

Together, the five configurations form a controlled ablation sequence that evaluates band-aware spectral-channel embedding, lightweight cross-channel attention, and NPV-weighted optimisation relative to the same U-Net spatial backbone. Detailed implementation information is provided in the GitHub repository, called *hyperFVC*, and available at `https://github.com/LNSOTOM/fvc_function`.

4.2. Experimental settings

4.2.1. Datasets, sites, and sensors

The experiments were conducted using the predictor–reference datasets described in Section 3.2. These datasets comprised multispectral and hyperspectral UAS image patches paired with BE, NPV, and PV reference masks. The multispectral configuration used the 5 cm multispectral predictor grid, whereas the hyperspectral configurations used the 10 cm FX10-only, FX17-only, and combined FX10–FX17 predictor grids. All experiments used sensor-specific masks aligned to the corresponding predictor rasters to ensure pixel-wise correspondence between input reflectance data and reference labels.

Within-site experiments used source-tile-level training, validation, and test partitions from the same annotated site to reduce spatial leakage among overlapping patches. Cross-site transferability was evaluated by applying selected trained models to an independent site, providing an external test of whether the learned spectral–spatial representations generalised beyond the annotated training domain.

4.2.2. Shared U-Net architecture and optimisation settings

All model variants used the same U-Net-style encoder–decoder backbone and training schedule; only the spectral modules and class-weighting settings differed across experiments. In the current implementation, the backbone used five encoder stages with feature depths of 64, 128, 256, 512, and 1024 channels, followed by a 2048-channel bottleneck. Each convolutional block used two 3×3 convolutional layers with batch normalisation, ReLU activation, and dropout. Downsampling was performed using 2×2 max pooling, and upsampling used 2×2 transposed convolutions followed by skip-feature concatenation. The final classifier used a 1×1 convolution to produce logits for the three FVC classes.

Models were trained using focal loss and the Adam optimiser. Invalid or unlabelled pixels were excluded from optimisation using an ignore index of -1. For unweighted experiments, the focal-loss alpha term was set to 1. For weighted experiments, class-specific alpha values were applied in the order BE, NPV, and PV; the default weighted setting was $[1, 2, 1]$, assigning a larger loss contribution to NPV. The shared architecture, optimisation, and training hyperparameters are summarised in Table 6.

Table 6: Shared U-Net architecture, optimisation, and training hyperparameters used across model variants. Input-channel dimensionality was sensor-dependent, while output classes, backbone structure, optimiser settings, and focal-loss form were kept consistent. The focal-loss alpha term differed only for the class-weighted variants.

Hyperparameter	Value
Input and output configuration	
Number of input channels	Sensor-dependent: 5 for selected multispectral inputs, 10 for full MICA multispectral inputs, 90 for FX17, 206 for FX10, and 296 for combined FX10–FX17 hyperspectral inputs
Number of output classes	3: BE, NPV, and PV
Output activation	Model returned logits; softmax was applied for probability-map interpretation and hard-class prediction
U-Net backbone architecture	
Encoder filter depths	64, 128, 256, 512 and 1024 channels
Bottleneck channels	2048 channels
Convolution kernel size	3×3
Final classifier kernel size	1×1 convolution
Pooling size	2×2 max pooling
Upsampling operation	2×2 transposed convolution
Dropout probability	0.3
Hidden activation function	ReLU in the CNN U-Net blocks
Spectral adapter activation	GELU when the spectral adapter was enabled
Optimisation and training settings	
Number of epochs	120
Batch size	4 patches per mini-batch by default; overridable through `BATCH_SIZE`
Gradient accumulation	2 mini-batches per optimiser step
Effective batch size	8 patches per optimiser step when `BATCH_SIZE` = 4
Optimiser	Adam with initial learning rate 1×10^{-4}, OneCycleLR scheduling, weight decay 1×10^{-4}, and beta parameters $(0.9, 0.999)$
Mixed precision	CUDA automatic mixed precision enabled by default during GPU training
AMP scaler	`GradScaler`, initial scale = 1024, growth interval = 2000
Gradient clipping	Maximum gradient norm = 1.0
Loss function and masking	
Loss function	Focal loss with focusing parameter $\gamma = 2$; invalid or unlabelled pixels were excluded using ignore index -1
Focal-loss alpha	1 for unweighted runs; class-weight vector for weighted runs, e.g., $[1, 2, 1]$ for BE, NPV, and PV

4.2.3. Training and inference protocols

All model variants used the same predictor-reference tiles, spatial data splits, optimiser settings, check-pointing criterion, and evaluation protocol. Only the enabled spectral modules, class-weighting setting, and sensor-

specific augmentation protocol differed across experiments. This design ensured that performance differences were attributable primarily to the architectural or loss-weighting components under evaluation rather than to differences in sample construction or training procedure.

Block-based data partitioning. Data were partitioned using a three-fold spatial block cross-validation strategy (Kattenborn et al., 2022; Sotomayor et al., 2025a). Annotated source tiles were grouped into spatial blocks, and one block was withheld as the independent test set in each fold. The remaining tiles were allocated to training and validation subsets using fixed tile-level counts. In the default configuration, 8 base tiles were used for training, 3 for validation, and 4 for testing, corresponding to 53.3%, 20.0%, and 26.7% of the 15 annotated base tiles, respectively. All patches derived from the same source tile were kept within the same split to prevent spatial leakage between training, validation, and test data. For the 9-patch-per-tile exports, this produced 72 training patches, 27 validation patches, and 36 test patches; lower patch-density exports preserved the same tile-level partitioning.

Patch generation. Training samples were generated by extracting paired image-mask patches from the reflectance products and corresponding BE, NPV, and PV reference masks. Patch size and stride followed the sensor-specific settings described in Section 3.2. Patches with insufficient valid pixels or dominated by NoData regions were excluded. The same patch-generation procedure was used for all model variants to preserve comparability across ablations.

Data augmentation. Data augmentation was applied to augmentation-enabled training profiles to improve generalisation and reduce overfitting under limited labelled data. A conservative core protocol was used for the hyperspectral FX10, FX17, and combined FX10–FX17 experiments, and also formed the base of the reported MICA multispectral configuration. This core protocol included horizontal flipping, vertical flipping, random rotations in 90° increments, and mild coherent brightness-contrast jitter. Geometric transformations were applied identically to predictor patches and PV/NPV/BE masks to preserve pixel-wise correspondence, whereas radiometric transformations were applied only to predictor reflectance patches. Invalid and unlabelled pixels were propagated through the augmentation pipeline and retained as ignore regions.

For the reported MICA configuration, the core augmentations were retained and additional shadow-robust radiometric perturbations were enabled for multispectral imagery. These additional transformations included global gain jitter, per-band gain jitter, gamma adjustment, mild Gaussian noise, and synthetic shadow patches. They were not applied to the FX10, FX17, or combined FX10–FX17 hyperspectral experiments because stronger radiometric perturbations can distort narrow-band spectral signatures important for hyperspectral classification. The augmentation protocols are summarised in Table 7.

Table 7: Data augmentation protocols used during model training. The core protocol was used for FX10, FX17, and combined FX10–FX17 hyperspectral experiments and formed the base of the reported MICA multispectral configuration. The MICA protocol added shadow-robust radiometric transformations for multispectral imagery only.

Protocol	Augmentation type	Operation	Probability
Core	Geometric	Horizontal flip	0.5
Core	Geometric	Vertical flip	0.5
Core	Geometric	Random rotation in 90° increments	0.5
Core	Radiometric	Mild coherent brightness–contrast jitter	0.5
MICA add-on	Radiometric	Global gain jitter	0.5
MICA add-on	Radiometric	Per-band gain jitter	0.5
MICA add-on	Radiometric	Gamma adjustment	0.35
MICA add-on	Radiometric	Mild Gaussian noise	0.2
MICA add-on	Shadow simulation	Synthetic shadow patches	0.35

Geometric transformations were applied identically to predictor patches and PV/NPV/BE masks. Radiometric and shadow-simulation transformations were applied only to predictor reflectance patches; reference masks were unchanged.

Class weighting. Class weighting was applied only to the weighted spectral-adapter variants, M3 and M5. The corresponding focal-loss alpha values are reported in Table 5 and described in Section 4.2.2.

Inference. For inference, the selected model checkpoint was first applied to held-out within-site test patches. Standard deterministic inference produced softmax probability maps and hard class predictions, with hard class maps used for metric calculation and qualitative map comparison. Monte Carlo Dropout inference was then performed separately as a post-inference diagnostic for uncertainty mapping, as described in Section 4.2.5. Finally, selected trained models were applied to independent-site predictor data for qualitative cross-site transfer assessment.

4.2.4. Evaluation metrics

Model performance was assessed using semantic segmentation metrics calculated from valid labelled pixels only. Invalid or unlabelled pixels with the ignore label -1 were excluded from all metric calculations. For each FVC class $c \in \{\mathrm{BE}, \mathrm{NPV}, \mathrm{PV}\}$, precision, recall, F1-score, and Intersection over Union (IoU) were calculated from the class-specific true positives (TP_c), false positives (FP_c), and false negatives (FN_c):

$$F1_c = \frac{2TP_c}{2TP_c + FP_c + FN_c}, \tag{1}$$

$$IoU_c = \frac{TP_c}{TP_c + FP_c + FN_c}. \tag{2}$$

The NPV F1-score was used as the primary target-class metric. Aggregate segmentation performance was summarised using macro averaged mean F1-score and mean IoU (mIoU) across BE, NPV, and PV:

$$\text{Mean F1} = \frac{F1_{\mathrm{BE}} + F1_{\mathrm{NPV}} + F1_{\mathrm{PV}}}{3}, \tag{3}$$

$$\text{mIoU} = \frac{IoU_{\mathrm{BE}} + IoU_{\mathrm{NPV}} + IoU_{\mathrm{PV}}}{3}. \tag{4}$$

Aggregate model-variant summaries were calculated by first computing metrics for each sensor-profile and patch-scale configuration, then averaging the corresponding configuration-level metrics by model variant. Detailed aggregation procedures are provided in Appendix A.

Within-site validation. Within-site validation assessed model performance on the independent test block withheld during the block-based partitioning procedure described in Section 4.2.3. This evaluation quantified BE, NPV, and PV segmentation performance across model variants, sensor profiles, and patch scales while avoiding leakage among patches derived from the same source tile.

4.2.5. Monte Carlo dropout uncertainty mapping

Monte Carlo dropout was used as a post-inference diagnostic to map pixel-wise epistemic uncertainty from the trained segmentation models (Gal and Ghahramani, 2016; Scheiter et al., 2022; Sotomayor et al., 2025a). Epistemic

uncertainty reflects incomplete model knowledge of the underlying data distribution and is relevant in semi-arid scenes where BE, NPV, PV, shadow, and mixed vegetation–soil backgrounds can be difficult to separate. Unlike aleatoric uncertainty, which is associated with intrinsic data noise, label ambiguity, or sensor variability, epistemic uncertainty can potentially be reduced through additional training data, improved model structure, or more representative spectral–spatial features.

Dropout layers with probability $p = 0.3$ were included in the segmentation network during training. For Monte Carlo dropout inference, model weights were fixed while dropout layers remained active, and each valid input patch was evaluated over $T = 50$ stochastic forward passes. Let $\mathcal{C} = \{\mathrm{BE}, \mathrm{NPV}, \mathrm{PV}\}$ denote the set of FVC classes, and let (i, j) denote the row and column location of a pixel within an image patch. For class $c \in \mathcal{C}$, the pre-softmax logit from stochastic pass t was denoted as $z_c^{(t)}(i, j)$.

Pixel-wise logit-space epistemic uncertainty was calculated as the mean class-wise standard deviation of the logits across stochastic passes:

$$U_{\mathrm{raw}}(i, j) = \frac{1}{|\mathcal{C}|} \sum_{c \in \mathcal{C}} \mathrm{SD}_{t=1}^{T} \left[z_c^{(t)}(i, j) \right], \tag{5}$$

where $|\mathcal{C}| = 3$ and $U_{\mathrm{raw}}(i, j)$ denotes the raw uncertainty assigned to pixel (i, j). This quantity represents logit-space prediction variability and was interpreted as a relative measure of model uncertainty, rather than as a calibrated probability of error.

Uncertainty was calculated only for valid input pixels. Invalid, nodata, and ignored pixels were excluded using the valid-data mask and written as missing values. Patch-level uncertainty outputs were stitched back into the orthomosaic coordinate grid using the same inference footprint as the deterministic class predictions, producing georeferenced uncertainty rasters aligned with the FVC prediction maps. Class-wise uncertainty summaries were calculated by averaging the unscaled U_{raw} values over valid pixels assigned to each predicted FVC class. The uncertainty rasters were used only as post-inference diagnostic layers and were not included in the deterministic accuracy metrics.

For comparative visualisation of the selected FX10–FX17 and MICA outputs, uncertainty maps were displayed using the same colour ramp and shared display limits of 0.10–0.65. Values outside these limits were clipped for display only. This display scaling affected only map rendering and did not

modify the underlying uncertainty values used for quantitative class-wise summaries.

4.2.6. Qualitative cross-site transfer inference

To examine transfer behaviour beyond the labelled training site, selected trained models were applied to an independent inference site. Because independent pixel-level reference labels were not available for this site, cross-site transfer was treated as qualitative inference rather than as a quantitative accuracy assessment. The resulting maps were used to compare spatial prediction patterns between the selected FX10–FX17 and MICA configurations and to visualise patch-scale differences for the FX10–FX17 model.

4.3. Post-inference spectral characterisation

Post-inference spectral characterisation was used to describe the spectral behaviour of pixels predicted as BE, NPV, and PV. The analysis combined reflectance-based class signatures, pairwise separability curves, spectral-index maps, and model-derived spectral-importance scores. Reflectance analyses were derived directly from the retained MICA and FX10–FX17 reflectance stacks, spectral indices were calculated from the retained FX10–FX17 reflectance bands, and importance scores were extracted from the trained spectral-encoding components.

4.3.1. Reflectance-based spectral response and class separability

Class-wise spectral responses were summarised from the retained reflectance stacks. Pixels predicted as BE, NPV, and PV were used as spatial masks, and reflectance values were extracted for each class across the available wavelength range. For each class and wavelength, mean reflectance responses were computed to describe the spectral profiles associated with the predicted FVC categories.

Pairwise separability between BE, NPV, and PV was calculated using standardised differences in class-wise mean reflectance responses. For each pair of classes and wavelength, the absolute class-mean difference was standardised to allow comparison across wavelengths and sensor profiles. The resulting curves were used to identify wavelength regions where predicted classes showed larger or smaller reflectance differences.

4.3.2. Post-inference spectral-index mapping

To complement the reflectance-based spectral response analysis, five spectral indices were derived from the nearest available FX10–FX17 reflectance bands (Table 8). This post-inference mapping step was used to extend interpretation beyond the predicted distribution of BE, NPV, and PV components by examining spatial variation in spectral proxies associated with vegetation physiological and biochemical traits, moisture or dry-material conditions, and exposed-substrate contribution within and across FVC classes. The selected indices represented greenness and photosynthetic activity, red-edge response, pigment transition, moisture or dry-material variation, and exposed-substrate contribution.

For representative inference tiles, each index was computed directly from the retained FX10–FX17 reflectance stack and mapped spatially. The predicted FVC class map was included only as a spatial reference for comparison with the spectral-index layers. The spectral-index maps were not derived from model logits, probabilities, or predicted class labels, and they were not used as model inputs. For visualisation, each index map was displayed using per-panel 2–98% percentile-normalised scaling to emphasise within-index spatial gradients; this display normalisation did not affect the index calculations or predicted class maps.

Table 8: Spectral indices used for post-inference spectral characterisation of the BE–NPV–PV continuum in the FX10–FX17 imagery. R_λ denotes reflectance at the nearest available band to wavelength λ nm.

Index	Formula	Main spectral proxy	Diagnostic use
kNDVI	$\tanh(\mathrm{NDVI}^2)$, where $\mathrm{NDVI} = \frac{R_{842}-R_{668}}{R_{842}+R_{668}}$	Greenness and photosynthetic activity	Spatial distribution of stronger or weaker vegetation greenness response.
NDRE	$\frac{R_{842}-R_{717}}{R_{842}+R_{717}}$	Red-edge response	Spatial distribution of chlorophyll-sensitive red-edge variation.
PSRI	$\frac{R_{668}-R_{560}}{R_{842}}$	Pigment transition	Spatial distribution of relative pigment-transition and senescence-sensitive response.
MSI	$\frac{R_{1597}}{R_{861}}$	SWIR–NIR moisture-sensitive contrast	Spatial distribution of dry-material or moisture-related variation.
BSI	$\frac{(R_{1597}+R_{668})-(R_{861}+R_{480})}{(R_{1597}+R_{668})+(R_{861}+R_{480})}$	Exposed substrate	Spatial distribution of bare-ground or substrate-background contribution.

4.3.3. Model-derived spectral importance analysis

Model-derived spectral importance analysis was used to summarise the wavelength regions assigned the highest relative importance by the trained spectral-encoding components. Class-wise importance scores were extracted by band or wavelength for the selected MICA and FX10–FX17 models. Scores were normalised within each class and sensor profile so that rankings represented relative spectral importance for a given model output rather than direct or absolute biophysical sensitivity.

The resulting importance rankings were interpreted alongside the reflectance-response and spectral-index analyses. Class-wise importance scores were treated as diagnostic model-output summaries rather than direct measure-

ments of vegetation traits or substrate properties.

4.4. Deployment workflow and edge benchmarking

The selected hyperspectral FX10–FX17 s152 and multispectral MICA s304 FVC segmentation models were exported from PyTorch to ONNX before TensorRT engine construction. The ONNX exports used dynamic batch and spatial dimensions, allowing inference over input tensors of size $N \times C \times H \times W$, where C denotes the number of spectral bands. Both exported models produced $N \times 3 \times H \times W$ logits corresponding to BE, NPV, and PV.

Although model training used automatic mixed precision (AMP), the ONNX exports retained FP32 weights. FP16 Reduced-precision execution was therefore introduced during TensorRT engine construction rather than inherited directly from the training configuration. Initial FP32 and pure FP16 TensorRT engines were built on Jetson AGX Orin hardware and benchmarked to characterise median latency, P99 latency, throughput, and serialized engine size. Inference latency was reported in milliseconds per tile, throughput was reported as tiles processed per second, and serialized engine size was reported in MiB.

Latency speed-up was calculated relative to the corresponding TensorRT FP32 baseline:

$$\text{Latency speed-up} = \frac{\text{FP32 median latency}}{\text{engine median latency}}.$$

Deployment consistency was evaluated by comparing ONNX Runtime and TensorRT outputs against the PyTorch reference on representative input patches. Parity assessment included logit differences, finite-logit checks, pixel-wise argmax agreement, and mIoU computed relative to the PyTorch argmax predictions across BE, NPV, and PV. TensorRT engines that produced non-finite logits were excluded from deployment interpretation.

Where pure FP16 execution was numerically unstable, Polygraphy precision debugging was used to construct mixed FP16/FP32 engines that preserved finite logits and high argmax agreement with the PyTorch reference. Unless stated otherwise, FP16-labelled TensorRT results refer to these validated mixed FP16/FP32 engines rather than pure FP16 engines. The final deployment comparison was therefore based only on finite-logit, parity-validated engines. The benchmark represents inference-stage edge deployment feasibility rather than a complete onboard UAS processing workflow.

5. Results

5.1. FVC classification performance across ablation experiments

5.1.1. Performance of baseline and spectrally structured models

Within-site ablation results differed across model variants (Table 9). M5 achieved the highest aggregate NPV F1-score, while M3 achieved the highest mean F1-score and mIoU. Compared with the baseline M1, M2 showed a small increase in NPV F1, mean F1, and mIoU. M4 produced similar aggregate values to M1. The largest increases in NPV F1 were observed for the NPV-weighted variants M3 and M5.

Table 9: Aggregate within-site performance across sensor-profile and patch-scale configurations for the five model variants. Values in parentheses indicate differences relative to M1.

Variant	NPV F1	Mean F1	mIoU
M1	0.348 (–)	0.701	0.597 (–)
M2	0.357 (+0.009)	0.706	0.604 (+0.007)
M3	0.490 (+0.142)	**0.745**	**0.629** (+0.032)
M4	0.345 (−0.003)	0.700	0.596 (−0.001)
M5	**0.496** (+0.148)	0.744	0.625 (+0.028)

Across individual sensor-profile and patch-scale combinations, the highest NPV F1-score was achieved by either M3 or M5 (Fig. 4). M5 was most frequently the highest-ranked variant for NPV F1-score, whereas M3 had slightly higher aggregate mean F1-score and mIoU. Additional diagnostics, including NPV IoU, mean F1-score, the NPV F1–mIoU trade-off, and class-wise BE–NPV–PV F1-score and IoU, are provided in Appendix A.

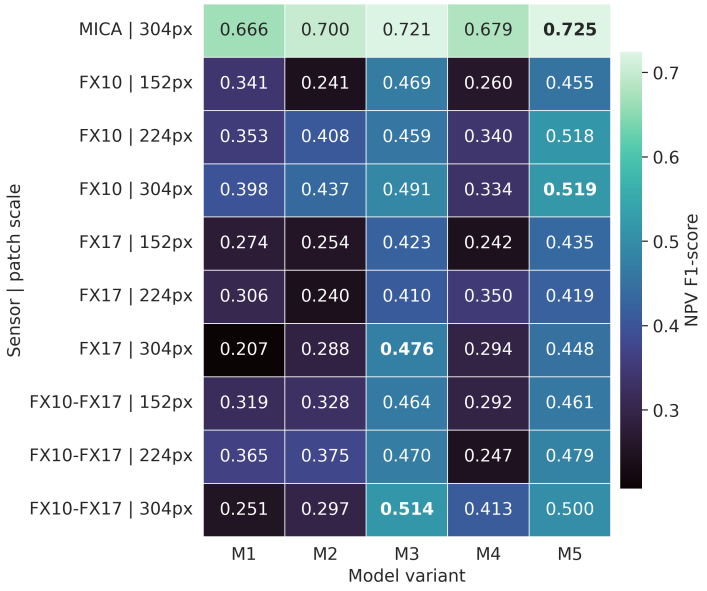

(a) NPV F1-score.

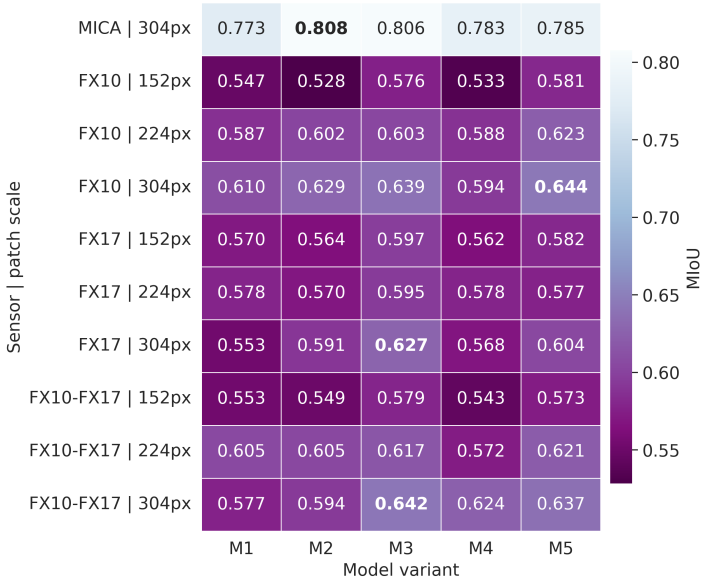

(b) mIoU.

Figure 4: Within-site segmentation performance across model variants, sensor profiles, and patch scales. Rows denote sensor-profile and patch-scale combinations, and columns denote model variants M1–M5. Bold values indicate the highest value within each sensor row.

Table 10 summarises the two configurations selected for subsequent qualitative, transferability, and edge-deployment analyses. The selected MICA configuration was M5 at 304 px, and the selected FX10–FX17 configuration was M5 at 152 px.

Table 10: Selected configurations used in subsequent qualitative, transferability, and edge-deployment analyses.

Sensors	Patch	Variant	NPV F1	NPV IoU	Mean F1	Role in analysis
MICA	304 px	M5	0.725	0.568	0.886	Spatial-resolution versus spectral-information comparison and Jetson edge benchmarking.
FX10–FX17	152 px	M5	0.462	0.300	0.705	Qualitative interpretation, cross-site transfer, and Jetson edge benchmarking.

Qualitative within-site inference was evaluated using tile 65, a mixed-cover tile containing BE–NPV–PV transitions and heterogeneous vegetation–background structure. The visual comparison included M1, M3, and M5 across patch scales of 152, 224, and 304 px.

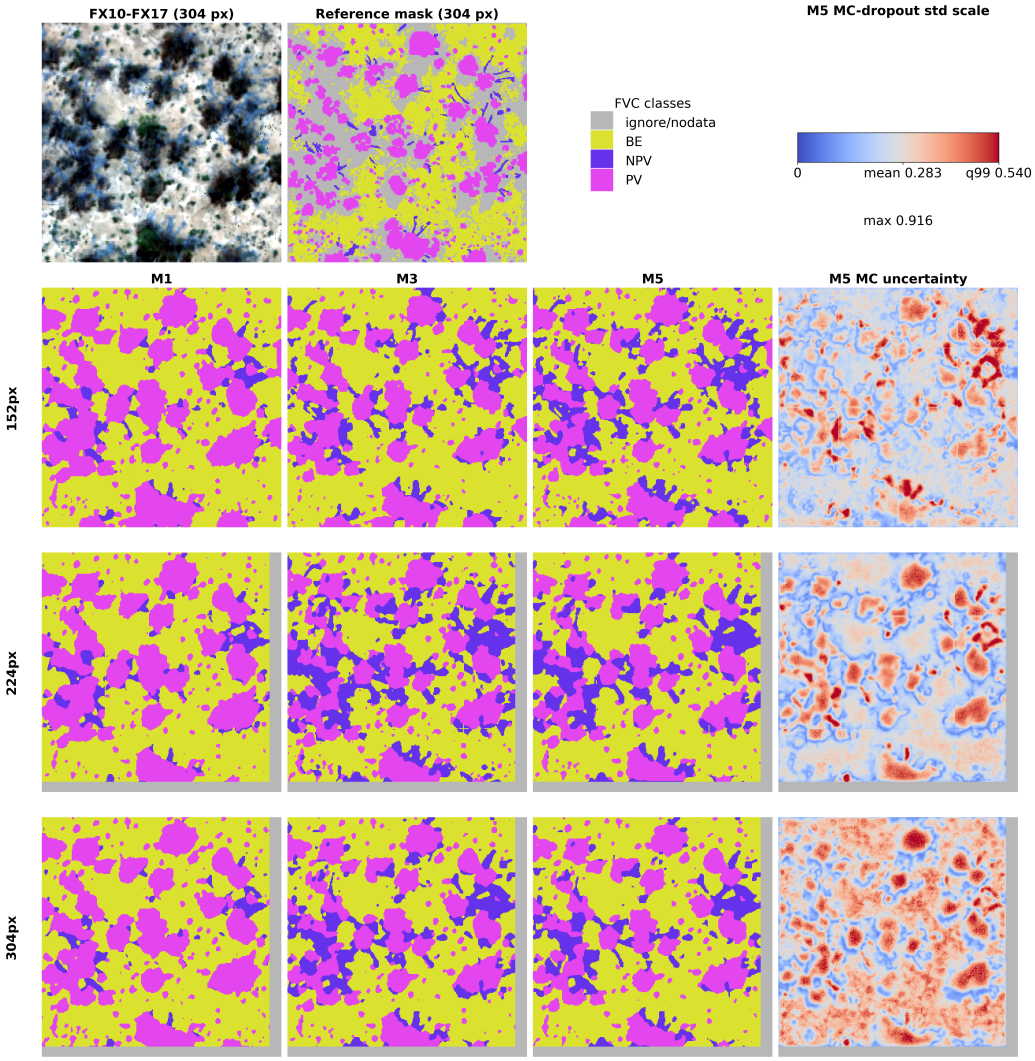

Figure 5: Within-site inference and epistemic uncertainty for tile 65 using the FX10–FX17 sensor profile. The top row shows the RGB composite, reference mask, FVC class legend, and M5 MC-dropout uncertainty scale. Prediction maps are shown for patch scales of 152, 224, and 304 px using model variants M1, M3, and M5. The final column shows M5 epistemic uncertainty at each patch scale, estimated from repeated stochastic MC-dropout predictions. Grey pixels denote ignore/nodata areas, and the uncertainty colour scale is clipped at the 99th percentile for visualisation.

The tile 65 predictions showed visible differences among model variants and patch scales. M3 and M5 produced more continuous NPV regions than M1. The 152 px outputs retained smaller spatial features, whereas the 224 px

and 304 px outputs appeared more spatially regularised. M5 uncertainty was concentrated around class-transition zones, mixed pixels, small vegetation fragments, and nodata-adjacent areas.

MICA and FX10–FX17 predictions were compared using approximately ground-footprint-matched display windows. The selected FX10–FX17 configuration was based on 152 px patches at 10 cm resolution, corresponding to approximately 15.2 m $\times$ 15.2 m on the ground. For visual comparison with the MICA output, the FX10–FX17 prediction was re-windowed to the same scene extent shown for the MICA 304 px, 5 cm configuration. Thus, both panels show comparable ground extents while retaining their native sensor-specific prediction outputs.

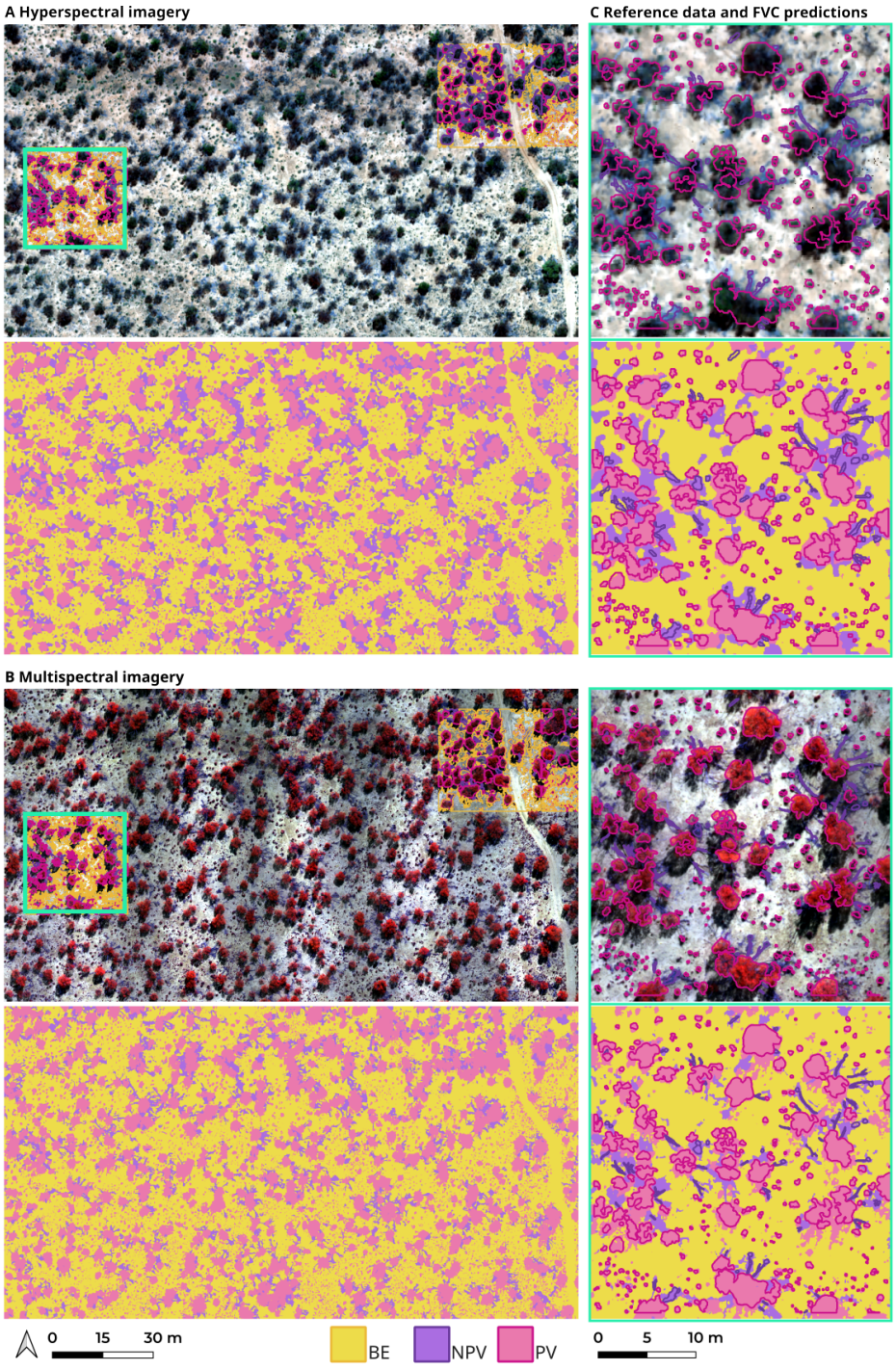

Figure 6: Ground-footprint-matched visual comparison of FX10–FX17 hyperspectral and MICA multispectral FVC inference. **A** FX10–FX17 imagery and FVC prediction from the selected 152 px configuration at 10 cm resolution, displayed over a 15.2 m × 15.2 m scene extent. **B** MICA imagery and FVC prediction from the selected 304 px configuration at 5 cm resolution, shown over the corresponding 15.2 m × 15.2 m scene extent. Reference annotations are overlaid on the imagery panels, and prediction panels show BE, NPV, and PV classes. **C** Enlarged subsets of the highlighted area show local correspondence between reference annotations and predicted FVC patterns.

Both outputs mapped the dominant BE, NPV, and PV patterns within the scene. Local differences were visible around mallee crowns, stem branches, and mixed bare-earth and litter-covered areas. To complement the class maps, Monte Carlo dropout uncertainty was used to compare the spatial structure of prediction stability between sensor configurations.

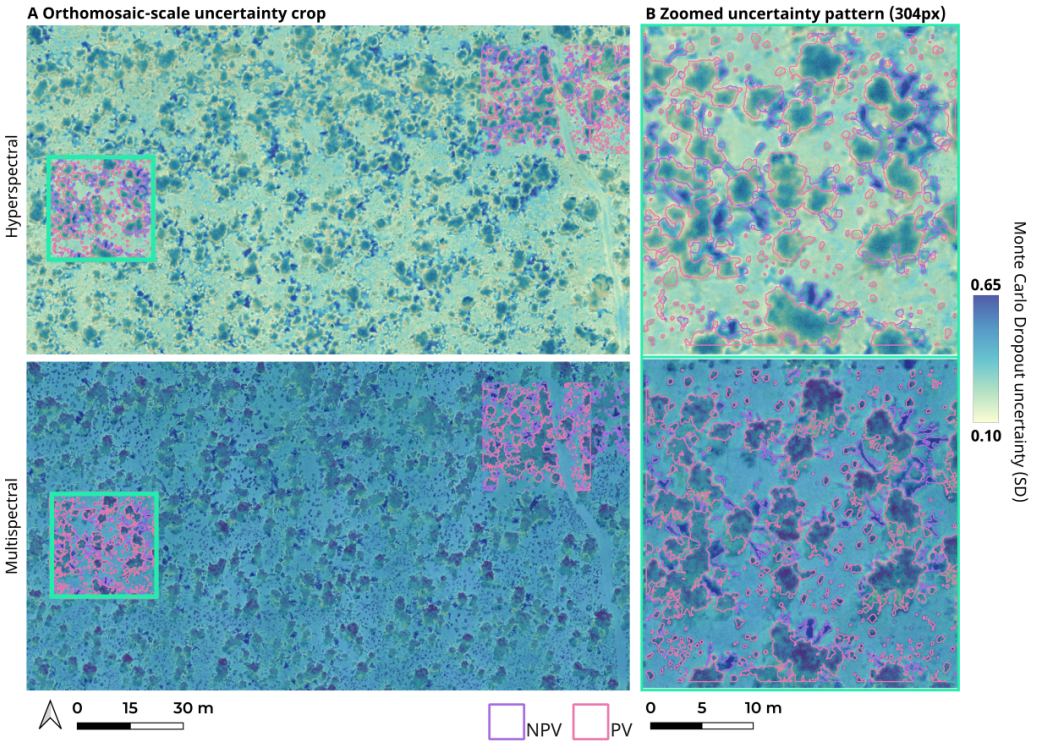

Figure 7: Epistemic uncertainty maps derived from Monte Carlo dropout inference for hyperspectral and multispectral FVC predictions. The top row shows the FX10–FX17 hyperspectral output at 10 cm spatial resolution, and the bottom row shows the MICA multispectral output at 5 cm spatial resolution. **A** shows an orthomosaic-scale uncertainty crop, while **B** shows the zoomed uncertainty pattern for the area indicated by the green inset box. Uncertainty was estimated as the pixel-wise mean class-wise standard deviation of pre-softmax logits across stochastic forward passes. Predicted NPV and PV boundaries are overlaid in purple and pink, respectively, for spatial interpretation. All uncertainty panels are displayed using the same colour ramp and shared display limits of 0.10–0.65, so colour intensity is directly comparable between the hyperspectral and multispectral outputs. Values outside these limits, where present, are clipped for display only.

The uncertainty maps showed sensor-specific spatial patterns under a common display scale. The FX10–FX17 hyperspectral output produced a

more spatially coherent uncertainty surface, with elevated values mainly aligned with transitions between vegetation cover and exposed bare ground or litter-covered surfaces, as well as heterogeneous shrub structure. In contrast, the MICA multispectral output retained finer object-level detail but showed greater local fragmentation in the uncertainty pattern. These spatial comparisons refer to the displayed crop, whereas the class-wise summaries were calculated from the full unscaled uncertainty rasters. Class-wise uncertainty summaries over the full orthomosaic showed that NPV had the highest Monte Carlo dropout standard deviation for both sensors, followed by PV and BE. For FX10–FX17, class-wise uncertainty was 0.0739 for BE, 0.1388 for NPV, and 0.0932 for PV. For MICA, the corresponding values were 0.0610 for BE, 0.1091 for NPV, and 0.0759 for PV. These summaries indicate that NPV was the least stable class across stochastic forward passes for both sensor configurations.

5.1.2. Cross-site transfer

Cross-site inference was evaluated at a new site using M5 configurations for FX10–FX17 and MICA (Fig. 8). Because reference labels were not available for this site, the outputs were interpreted qualitatively. For FX10–FX17, the selected 152 px output was shown together with the 304 px output for the same highlighted subset to visualise patch-scale differences. The MICA 304 px output was included as the corresponding multispectral comparison.

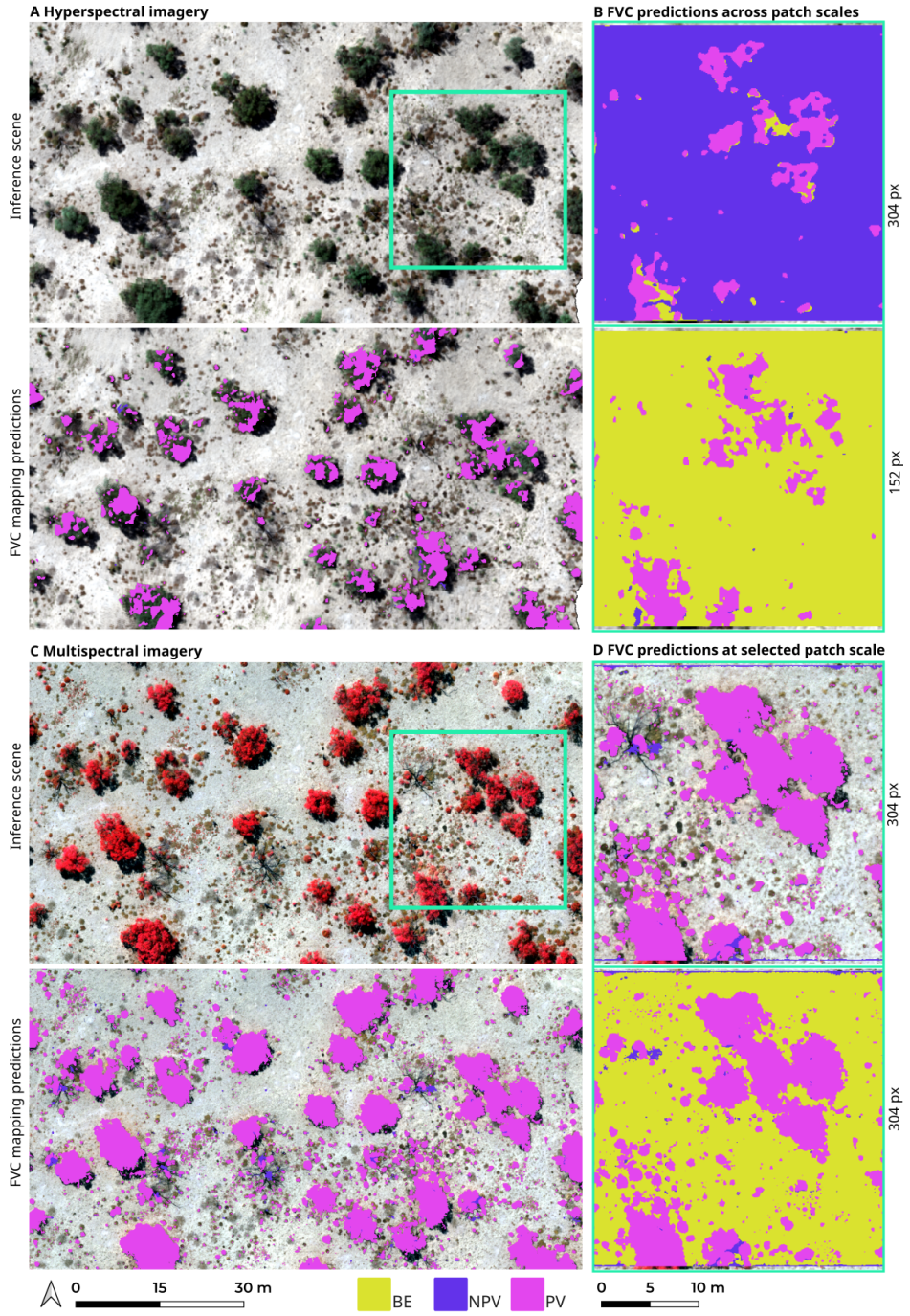

Figure 8: Cross-site FVC inference examples for M5 configurations using FX10–FX17 hyperspectral and MICA multispectral inputs. **A** New-site FX10–FX17 imagery and FVC prediction for the wider inference scene. **B** Enlarged FX10–FX17 subset showing predictions from the 304 px and 152 px patch-scale configurations. **C** New site MICA imagery and FVC prediction for the corresponding multispectral scene. **D** Enlarged MICA subset showing the 304 px prediction at the selected patch scale. Cyan boxes indicate the subset locations shown in the enlarged panels. Prediction panels show BE, NPV, and PV classes.

The FX10–FX17 152 px and 304 px outputs showed contrasting BE–NPV behaviour within the highlighted subset. The 152 px output preserved more local structure and showed less apparent mixing between BE and NPV, mapping much of the bright exposed bare ground as BE while retaining localised NPV and PV patches. In contrast, the 304 px output appeared to confuse BE and NPV over much of the highlighted subset, assigning the same bright exposed bare ground areas largely to NPV and producing a broad contiguous NPV-dominated region. This pattern suggests that the larger FX10–FX17 patch scale overgeneralised NPV in the unlabelled cross-site inference scene, rather than indicating a reliable increase in mapped NPV cover. The MICA 304 px output provided the multispectral comparison for the same cross-site inference context, but no quantitative accuracy comparison was made because independent reference labels were unavailable.

5.2. Spectral characterisation of predicted FVC classes

The spectral characterisation results are presented in the same order as the post-inference analyses. First, class-wise reflectance signatures and pairwise separability describe spectral differences among predicted BE, NPV, and PV pixels. Second, spectral-index maps show the spatial distribution of selected vegetation- and substrate-sensitive spectral proxies within a representative inference tile. Third, class-wise spectral-importance rankings summarise the wavelength regions assigned the highest relative importance by the selected models.

5.2.1. Reflectance response and class separability

The class-wise reflectance analysis showed distinct but partially overlapping spectral responses for BE, NPV, and PV across the MICA and FX10–FX17 datasets (Fig. 9). BE generally had higher reflectance than the vegetation classes, particularly across the red-edge, NIR, and SWIR regions. In the MICA data, PV had lower reflectance than NPV in the visible and red-edge bands, but higher reflectance in the NIR band. In the FX10–FX17 data, PV and NPV showed similar reflectance across parts of the red-edge and NIR transition, with greater separation in selected SWIR wavelengths.

Pairwise separability varied by wavelength. In the MICA data, BE–PV and BE–NPV differences were largest across the visible to red-edge wavelengths, whereas NPV–PV differences were smaller near the red-edge/NIR transition. In the FX10–FX17 data, BE–PV differences were high across

much of the VNIR–SWIR range and increased again at longer SWIR wavelengths. BE–NPV differences were largest in the visible to red-edge region and decreased through parts of the NIR–SWIR range. NPV–PV differences were lowest across parts of the red-edge and NIR, but increased in selected SWIR wavelengths.

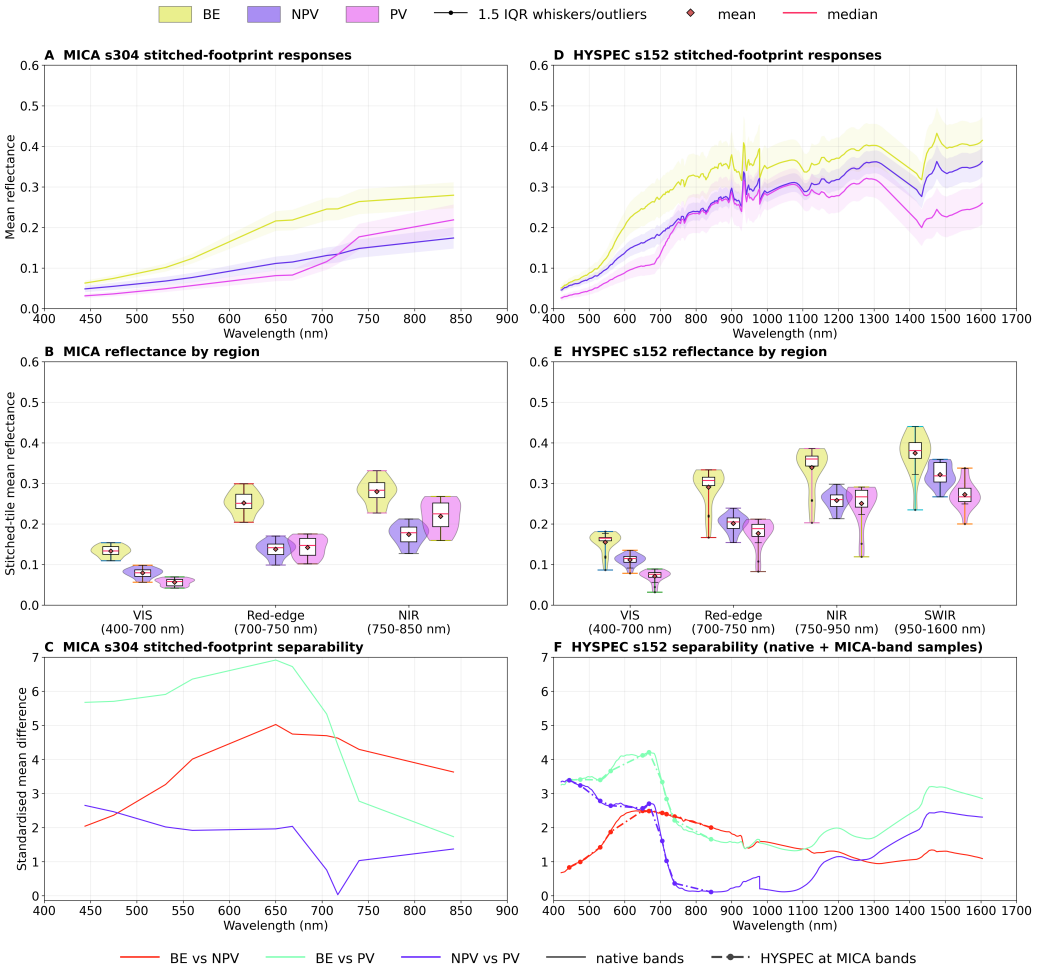

Figure 9: Class-wise spectral response, regional reflectance, and pairwise separability of predicted FVC classes derived from reflectance values. **A** and **D** show mean reflectance signatures for BE, NPV, and PV for the MICA and FX10–FX17 datasets, respectively. **B** and **E** summarise class-wise reflectance distributions by broad spectral region. **C** and **F** show standardised pairwise mean differences across wavelength. In **F**, solid lines show native FX10–FX17 bands and point markers indicate the nearest FX10–FX17 samples to the MICA band positions.

5.2.2. Spectral-index maps in inference tiles

The post-inference spectral-index maps showed distinct spatial patterns relative to the predicted FVC classes in the representative FX10–FX17 inference tile (Fig. 10). kNDVI and NDRE showed higher relative values over shrub crowns and PV-dominated prediction regions, consistent with stronger greenness, photosynthetic activity, and red-edge responses. PSRI and MSI showed higher relative values in areas associated with dry vegetation, litter-covered ground, and mixed vegetation background surfaces, consistent with pigment-transition and moisture or dry-material variation. BSI showed higher relative values over exposed substrate and BE-dominated prediction regions. The strongest spatial contrasts occurred around shrub boundaries and mixed BE–NPV–PV areas, where the index maps highlighted fine-scale transitions between live vegetation, dry vegetation, and exposed background.

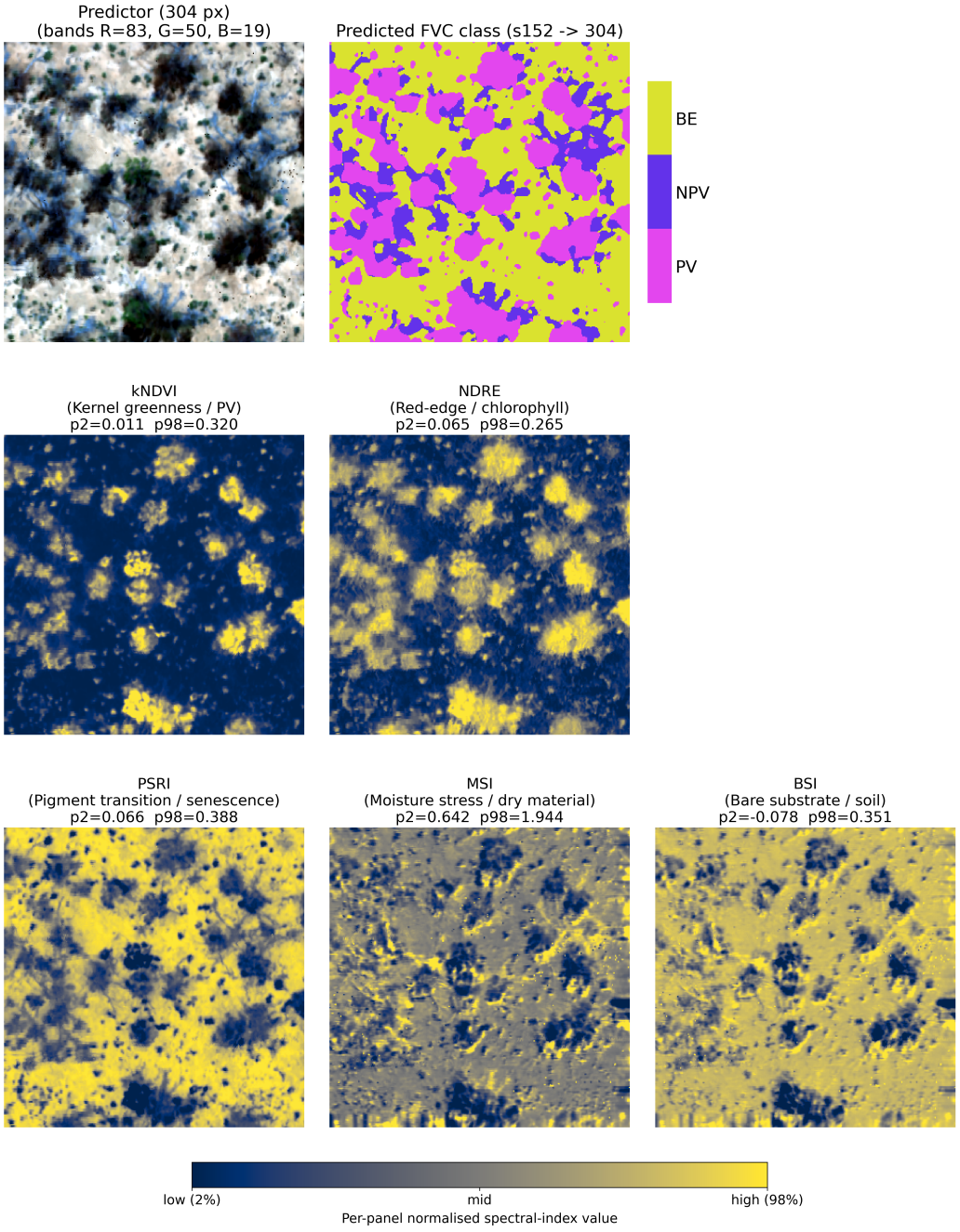

Figure 10: Representative FX10–FX17 inference tile showing the false-colour predictor, predicted FVC class map, and post-inference spectral-index maps. The predicted FVC map shows BE, NPV, and PV classes. Spectral-index maps were calculated from the retained reflectance bands and displayed using per-panel 2–98% percentile-normalised scaling. Colours indicate relative low-to-high values within each index map and are not directly comparable between indices.

5.2.3. Model-derived spectral importance

Class-wise spectral-importance rankings varied between the MICA and FX10–FX17 models (Fig. 11). For MICA, the highest-ranked bands for BE, NPV, and PV were centred in the red, red-edge, and NIR regions, including wavelengths near 668, 705, 717, 740, and 842 nm. For FX10–FX17, the highest-ranked wavelengths were concentrated mainly in the NIR–SWIR range. BE importance was highest at longer SWIR wavelengths, particularly around 1476–1590 nm. PV and NPV importance was concentrated mainly around 1265–1321 nm, with NPV also showing high importance near 1476 nm. These rankings were interpreted as relative model-derived wavelength-importance summaries rather than direct measures of vegetation or substrate biophysical properties.

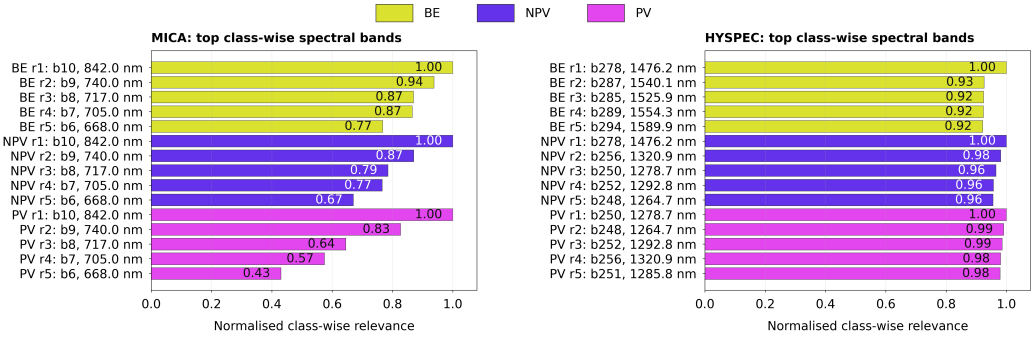

Figure 11: Top class-wise spectral-importance bands and wavelengths for BE, NPV, and PV predictions. Importance scores were normalised within each class and sensor profile. The MICA rankings show the highest-ranked multispectral bands, and the FX10–FX17 rankings show the highest-ranked hyperspectral wavelengths for each predicted class.

5.3. Edge deployment performance

ONNX Runtime reproduced the PyTorch outputs exactly within the reported precision for both sensors, with 100.00% argmax agreement and mIoU of 1.00. TensorRT FP32 also preserved the PyTorch predictions, with 100.00% agreement for FX10–FX17 s152 and near-perfect agreement for MICA s304. Pure FP16 TensorRT engines produced non-finite logits and were therefore not considered deployment-ready. The validated FP16-labelled TensorRT engines produced larger logit differences, as expected from reduced-precision execution, but maintained high argmax consistency with the PyTorch reference.

Table 11: TensorRT edge-deployment summary for the selected FVC segmentation models on Jetson AGX Orin. Engine size refers to the serialized TensorRT engine footprint. Agreement and mIoU were computed relative to the PyTorch argmax predictions. Latency speed-up was calculated relative to the corresponding TensorRT FP32 median latency. FP16-labelled rows correspond to validated mixed FP16/FP32 TensorRT engines rather than pure FP16 engines. Full logit-level and argmax-level parity diagnostics are provided in Supplementary Table Appendix B.2.

Sensor	**Engine**	**Size (MiB)**	**Latency (ms)**	**Throughput (tiles s^{-1})**	**Speed-up (×)**	**Agree (%)**	**mIoU**
FX10–FX17 s152	TRT FP32	133.77	16.31	65.51	1.00	100.00	1.00
FX10–FX17 s152	TRT FP16	93.71	9.62	116.02	1.70	99.96	1.00
MICA s304	TRT FP32	159.89	46.71	21.42	1.00	100.00	1.00
MICA s304	TRT FP16	204.70	52.05	19.22	0.90	99.99	1.00

For the FX10–FX17 s152 model, the validated FP16-labelled TensorRT engine reduced median per-tile latency from 16.31 to 9.62 ms, increased throughput from 65.51 to 116.02 tiles s^{-1}, and preserved 99.96% argmax agreement with the PyTorch reference. This represented a 1.70× latency speed-up and reduced the serialized engine footprint from 133.77 to 93.71 MiB.

In contrast, the MICA s304 FP16-labelled engine was slower than its FP32 baseline. Median latency increased from 46.71 to 52.05 ms, throughput decreased from 21.42 to 19.22 tiles s^{-1}, and the serialized engine footprint increased from 159.89 to 204.70 MiB. Although prediction parity remained high, the FP16-labelled configuration did not provide a deployment advantage for this model.

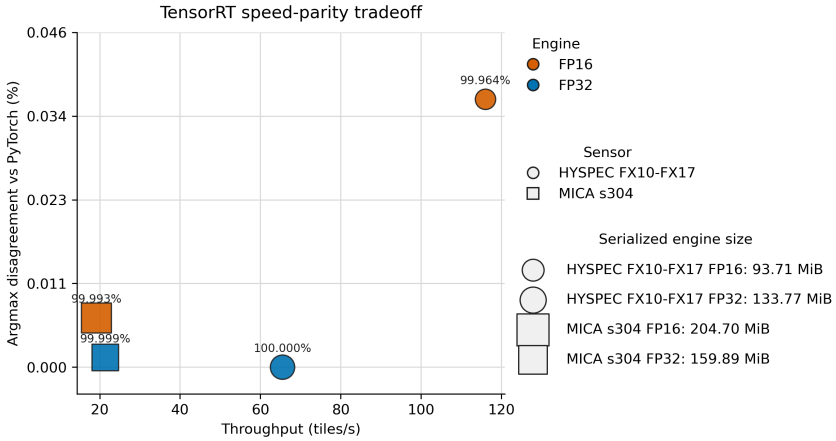

Figure 12: TensorRT speed–parity trade-off on Jetson AGX Orin. The x-axis shows throughput in tiles s^{-1}, and the y-axis shows argmax disagreement relative to the PyTorch reference, computed as 100−pixel-wise agreement. Marker colour denotes TensorRT engine precision, marker shape denotes sensor, and marker size indicates serialized engine size. Text labels show pixel-wise agreement with PyTorch. Points closer to the lower-right indicate higher throughput with stronger prediction parity.

Together, the deployment results show that TensorRT precision selection was model dependent. FP16-labelled mixed precision improved latency, throughput, and engine size for the hyperspectral FX10–FX17 s152 model while preserving high prediction parity with PyTorch. For the multispectral MICA s304 model, FP32 remained the preferred deployment configuration because it provided lower latency, higher throughput, smaller engine size, and marginally stronger agreement with the PyTorch reference. Detailed ONNX export metadata, TensorRT engine validation status, full parity diagnostics, supplementary latency-throughput diagnostics, and representative tile-level parity maps are provided in Appendix B.

6. Discussion

6.1. NPV-aware FVC segmentation and PV–NPV discrimination

We demonstrated an NPV-aware, spectrally structured CNN workflow for mapping fractional vegetation cover from multi-sensor UAS optical imagery in semi-arid vegetation. This addresses a central challenge in dryland remote sensing: although PV, NPV, and BE are all ecologically meaningful components of vegetation cover, NPV is often the most difficult to map because it comprises dry or senescent vegetation, litter, coarse woody debris,

and standing dead woody material, whose spectral and spatial characteristics can overlap with shadows, exposed substrate, and mixed vegetation–soil pixels (Lewis et al., 2001; Fisk et al., 2019a; Melville et al., 2019a; Li et al., 2023; Sotomayor et al., 2025a). By extending a U-Net-based FVC segmentation framework with band-aware spectral encoding, NPV-weighted optimisation, data augmentation, and patch-scale evaluation, the workflow provides a controlled basis for assessing how model design, class imbalance, spatial context, training variability, and sensor configuration affect PV–NPV–BE discrimination.

The ablation results show that improved PV–NPV discrimination was driven more by the interaction between spectral encoding and NPV-aware optimisation than by model complexity alone. The largest gains in NPV F1-score were obtained by the NPV-weighted variants, M3 and M5, whereas the unweighted spectral-adapter and unweighted transformer variants remained close to the baseline. This indicates that band-aware spectral encoding was most useful when coupled with a loss function that explicitly increased the contribution of the spectrally ambiguous NPV class.

The spectral adapter provided the main band-aware projection before spatial decoding. By using an SE-reweighted 1×1 convolutional stem, the spectral-adapter stem allowed the network to learn sensor-specific channel combinations before passing the representation to the U-Net encoder–decoder. This was particularly relevant for multi-sensor FVC mapping because MICA and FX10–FX17 differed strongly in spectral dimensionality, wavelength coverage, and spatial support. The lightweight spectral transformer extended this representation by modelling global cross-channel interactions within the learned spectral embedding. However, the aggregate difference between M3 and M5 was small, indicating that the additional transformer component provided only a modest gain relative to the effect of NPV weighting. The spectral adapter and lightweight transformer are therefore best interpreted as supporting components within a class-weighted segmentation framework, rather than as independent solutions to NPV ambiguity. This finding is consistent with the broader view that UAS vegetation segmentation benefits from architectures that balance spatial feature learning, annotation efficiency, and sensor-specific spectral representation, rather than relying only on increasingly complex models (Kattenborn et al., 2019a, 2021; Chowdhury et al., 2026).

This behaviour reflects the structure of the FVC classification problem in semi-arid vegetation. PV and BE were generally more separable because

they represent more distinct vegetation and substrate conditions, whereas NPV occupied an intermediate spectral and spatial position between photosynthetically active vegetation and exposed background. NPV included dry or senescent vegetation, litter, coarse woody debris, and standing dead woody material, which can overlap spectrally and spatially with shadows, exposed substrate, and mixed vegetation–soil pixels. Under these conditions, class weighting increased sensitivity to NPV omission, but also introduced trade-offs with more dominant or separable classes. This explains why M5 achieved the highest aggregate NPV F1-score, while M3 achieved the highest mean F1-score and mIoU.

The comparison between MICA and FX10–FX17 highlights a central spatial–spectral trade-off for transfer-oriented FVC mapping. MICA provided finer spatial detail, which supported sharper segmentation of object boundaries, small vegetation patches, and mixed BE–NPV–PV surface components. This interpretation is conceptually consistent with UAS-based CNN studies showing that high spatial resolution can be important for resolving fine vegetation classes and spatial patterns, although the degree of benefit depends on the spectral and spatial separability of the target classes, the surrounding spatial context, and reference data balance (Kattenborn et al., 2019a; Schiefer et al., 2020). In contrast, FX10–FX17 provided broader VNIR–SWIR spectral information, which was less advantageous for fine boundary delineation but more informative for interpreting dry vegetation, substrate mixtures, and moisture-sensitive spectral variation. Thus, the multispectral configuration was more effective for high-resolution within-site segmentation, whereas the imaging spectroscopy configuration provided a stronger diagnostic basis for interpreting why NPV remained difficult to separate from PV and BE.

The Monte Carlo dropout uncertainty maps provided an additional diagnostic of this spatial–spectral trade-off. Although the selected MICA configuration achieved stronger within-site segmentation metrics, its uncertainty surface was more locally fragmented, consistent with finer 5 cm spatial sampling and greater sensitivity to object-level boundaries, shadows, branches, and mixed vegetation–soil structure. In contrast, the FX10–FX17 output showed a more spatially coherent uncertainty structure despite its coarser 10 cm resolution, suggesting that broader VNIR–SWIR spectral information helped organise model confidence around ecologically plausible transition zones. Together, the metric results, visual inference, and uncertainty maps show that PV–NPV discrimination depends on the combined effects of

spatial resolution, broader spectral information, class-weighted optimisation, and local surface heterogeneity.

Patch-scale effects further shaped the relationship between quantitative performance and spatial prediction quality. Here, patch scale refers to the UAS input tile or image patch used for segmentation, where the 304 px and 152 px configurations represented different spatial-context windows. The larger 304 px input patch produced stronger aggregate metrics, suggesting that broader spatial context helped stabilise class assignment and reduce local prediction noise. In contrast, qualitative inference showed that the smaller 152 px input patch better preserved fine-scale BE–NPV–PV structure, including small NPV fragments, vegetation–soil mixtures, and local class boundaries. This indicates that higher aggregate metrics do not necessarily produce more spatially detailed or ecologically faithful maps. Larger patches may regularise predictions by integrating surrounding context, whereas smaller patches may retain local surface heterogeneity at the expense of broader contextual information. This interpretation is consistent with recent high-resolution aerial/UAS imagery and hyperspectral segmentation studies showing that scale selection affects both spatial context and segmentation detail. For example, Möhring et al. (2025) used fixed 1024×1024 px tiles, demonstrating that tile size and image resolution jointly determine the real-world spatial context available to the model, while Braham et al. (2025) showed that reduced patch or token scales can improve segmentation detail by preserving rich pixel-level spectral information. However, this comparison should be made cautiously because the present study evaluates UAS input patch scale, whereas internal transformer token size was evaluated by Braham et al. (2025).

Data augmentation likely supported robustness to illumination and spatial variability during training by increasing variation in object orientation, patch composition, brightness, contrast, and shadow conditions. This interpretation is consistent with previous CNN-based vegetation remote sensing studies that emphasise the importance of training-data diversity and augmentation for improving generalisation in high-resolution UAS imagery (Kattenborn et al., 2019a; Schiefer et al., 2020; Möhring et al., 2025; Sotomayor et al., 2025a). This is particularly relevant for semi-arid FVC mapping because BE, NPV, and PV can have subtle class separability under variable illumination, canopy shadow, and soil-background conditions. However, because augmentation was included as part of the training protocol rather than tested as an independent ablation factor, its effect should be interpreted as a

contributor to model robustness rather than as a separately quantified driver of performance.

Cross-site inference extended the evaluation beyond the labelled training domain. Because reference labels were not available for the new site, this analysis should be interpreted as qualitative transfer inference rather than externally validated accuracy assessment. Nevertheless, comparing selected M5 configurations and FX10–FX17 patch scales provided a practical transfer diagnostic by showing how model choices affected spatial prediction structure under new site conditions. This supports the use of the ablation framework as a model-selection step before future externally validated transfer experiments.

6.2. Spectral characterisation and model interpretability

The post-inference spectral characterisation workflow provided diagnostic evidence for interpreting CNN-predicted FVC classes, with particular emphasis on the spectrally ambiguous NPV component. Although CNNs can exploit spatial–spectral patterns for BE–NPV–PV segmentation, their predictions require additional interpretation when classes include mixed or transitional materials. By combining class-wise reflectance signatures, pairwise spectral separability, post-inference spectral-index maps, Monte Carlo dropout-based uncertainty, and class-wise model-derived spectral importance scores, the workflow linked predicted BE, NPV, and PV patterns to observable spectral behaviour.

The post-inference spectral analysis was most useful for explaining why NPV remained difficult, rather than simply confirming which model achieved the highest segmentation accuracy. In the MICA data, class differences were concentrated mainly in the visible, red-edge, and NIR bands. These regions provide contrast related to greenness, chlorophyll-sensitive response, canopy scattering, and vegetation–substrate separation (Homolová et al., 2013; Melville et al., 2019a; Sotomayor et al., 2025a). This helps explain the strong within-site performance of the high-resolution multispectral configuration. However, VIS–NIR information alone does not uniquely isolate dry vegetation material, particularly where NPV overlaps with exposed soil, woody debris, shadows, and mixed vegetation–soil backgrounds. Therefore, strong multispectral segmentation performance should not be interpreted as evidence that NPV is spectrally unambiguous in the VIS–NIR domain.

The FX10–FX17 results extended the diagnostic evidence into the SWIR, where reflectance responses, pairwise separability, and model-derived spectral-

importance scores provided additional contrast for NPV and substrate-related mixtures. Because the FX10–FX17 predictions were generated at the stitched-footprint support, spectral separability was interpreted primarily at the same prediction scale. Native hyperspectral pixels can describe finer-scale spectral variability, but they were not treated as the primary basis for explaining prediction-scale class separability. This distinction is important because separability estimated at the native hyperspectral pixel scale may reflect intrinsic spectral detail that is not fully preserved in the stitched prediction units.

Model-derived spectral importance was elevated around 1265–1321 nm and 1476–1590 nm, regions consistent with known dry-material, water-sensitive, substrate-related, and senescence-associated spectral responses (Lewis et al., 2001; Homolová et al., 2013; Turner et al., 2023; Haynes et al., 2026). These patterns should be interpreted cautiously. The spectral-importance scores indicate wavelength regions that contributed to model discrimination, but they do not show that the model directly retrieved vegetation physiological traits. Therefore, the attention and band-relevance outputs are best treated as diagnostic summaries of model behaviour that are consistent with known senescence-related and moisture-sensitive spectral regions.

The MICA versus FX10–FX17 comparison therefore provides a clear interpretation of the sensor trade-off. High-resolution multispectral imagery supported strong segmentation because the CNN could exploit colour, texture, object boundaries, and neighbourhood context. Broader VNIR–SWIR imaging spectroscopy data provided complementary information for interpreting dry vegetation, substrate mixtures, and class transitions, even when they did not produce the strongest fine-scale segmentation. The main interpretation from this subsection is that broader spectral information improved the interpretability of PV–NPV–BE ambiguity, whereas finer spatial detail improved map sharpness and within-site segmentation.

6.3. Edge deployment feasibility for UAS-based FVC mapping

We demonstrated that selected MICA and FX10–FX17 FVC segmentation models could be moved from the training environment to embedded GPU inference. Both models were exported to ONNX, optimised with TensorRT, and benchmarked on Jetson AGX Orin hardware. This addresses the operational requirement that dense tiled inference over high-resolution multispectral and imaging spectroscopy mosaics should be computationally feasible outside a workstation environment.

The deployment results show that edge readiness depends on more than segmentation accuracy. Numerical consistency between the native model and the exported inference engine is required to ensure that optimisation does not alter class predictions. In addition, latency, throughput, model footprint, and precision mode determine whether tiled inference is practical on portable GPU hardware. The successful deployment of the higher-dimensional FX10–FX17 model indicates that spectrally structured FVC segmentation can remain operationally feasible even when the input contains hundreds of spectral bands.

These results demonstrate edge-deployment feasibility by showing that the selected multispectral and imaging spectroscopy models can be converted into deployable inference engines without losing numerical consistency. However, the benchmark should be interpreted as an edge-inference feasibility test rather than a complete onboard autonomy workflow. A field-ready system would still require integration with radiometric correction, georeferencing, tiling, valid-data masking, mosaicking, uncertainty mapping, and mission-level data handling under realistic power, memory, and acquisition constraints. These requirements are consistent with recent work on onboard and edge AI for drone remote sensing, optimised inference on NVIDIA Jetson platforms, and low-compute hyperspectral models for remote-sensing applications (Koubaa et al., 2023; Mittal, 2019; López-Fandiño et al., 2024; Růžička and Markham, 2024).

6.4. Limitations and future transfer

This study provides a controlled and sensor-informed baseline for NPV-focused UAS FVC mapping in heterogeneous semi-arid ecosystems. The workflow integrates spectrally structured CNN variants, NPV-weighted optimisation, post-inference spectral characterisation, uncertainty mapping, and edge benchmarking. However, several limitations should temper the interpretation of the results and guide future transfer, upscaling, and operational deployment.

Within-site evaluation and qualitative cross-site transfer. First, quantitative evaluation was based on within-site labelled data, whereas cross-site inference was qualitative because independent reference labels were not available for the new site. The independent-site outputs therefore show spatial prediction behaviour under new site conditions, but they should not be interpreted as

externally validated accuracy. Future work should include labelled independent sites to quantify transferability using class-wise F1-score, IoU, confusion matrices, and uncertainty calibration.

NPV class heterogeneity and uncertainty validation. Second, NPV remained the main ecological and modelling challenge because it grouped dry grasses, senescent vegetation, litter, woody debris, and standing dead material into a single class. This grouping is appropriate for FVC mapping, but it limits diagnosis of which NPV subcomponents drive model errors, uncertainty patterns, or spectral-importance rankings. Future work could use hierarchical labels or targeted NPV subclasses where sufficient reference data are available, such as the labels provided by Sotomayor et al. (2025c). Externally labelled datasets would also allow Monte Carlo dropout-based uncertainty to be evaluated against observed misclassification, boundary disagreement, and class-specific error rates, supporting stronger use of uncertainty layers for quality control, active learning, and targeted field validation.

Sensor harmonisation and spatial–spectral transferability. Third, the comparison between MICA and FX10–FX17 reflects coupled differences in spatial resolution, spectral dimensionality, signal-to-noise ratio, acquisition geometry, and co-registration uncertainty. Although the ground-footprint-matched comparison supported visual interpretation over similar scene extents, it did not fully isolate these sensor effects. Future sensor-harmonised experiments using matched spatial resolutions, controlled band subsets, and common spatial footprints would help clarify when high spatial resolution improves boundary agreement and when VNIR–SWIR information improves separation of spectrally ambiguous NPV, PV, and BE mixtures. Therefore, transferability across sites, seasons, sensors, and spatial supports requires further testing before the framework is generalised to broader operational monitoring.

Pretrained transfer and foundation-model adaptation. Finally, pretrained transfer learning and foundation-model adaptation remain important directions for reducing annotation requirements and improving cross-site generalisation, although they were not evaluated in this study (Kattenborn et al., 2021; Chowdhury et al., 2026). Recent hyperspectral adapter studies have explored adapting RGB-pretrained or foundation-model backbones to hyperspectral imagery using spectral transformers, spectral priors, or spectral

convolutional adapters (Braham et al., 2025; Hurtado et al., 2025). In contrast, the variants evaluated here used a task-specific U-Net with an SE-reweighted 1×1-convolutional spectral stem and optional lightweight global cross-channel attention. This provides a controlled NPV-aware baseline for future comparison with larger pretrained or foundation-model adaptation frameworks.

Future transfer domains and operational scaling. Future transfer should first prioritise multi-site and multi-season semi-arid rangeland datasets spanning gradients in vegetation condition, soil background, illumination, and phenology. Once validated across these gradients, the framework could be tested in structurally and spectrally different ecosystems where PV–NPV–BE mixtures differ from the original training domain, including Antarctic moss and lichen communities, alpine tundra, dry coastal heathlands, post-fire landscapes, arid shrublands, and other environments with strong moisture gradients, exposed substrate, senescent material, and mixed vegetation–soil backgrounds. Scaling to broader monitoring contexts will require harmonisation across sensors, platforms, and spatial resolutions, including matched-resolution experiments, UAS-to-airborne or UAS-to-satellite calibration strategies (Schiefer et al., 2023), and domain-adaptation or radiative-transfer approaches to separate vegetation spectral signals from platform-specific effects (Guanter et al., 2015; Chabrillat et al., 2024; Reddig et al., 2025; Haynes et al., 2026). In parallel, edge deployment should move beyond inference benchmarking toward complete field workflows integrating radiometric correction, tiling, masking, model inference, uncertainty mapping, and geospatial mosaicking under realistic UAS power, memory, and storage constraints.

7. Conclusions

This study developed and evaluated an NPV-aware, spectrally structured CNN workflow for UAS-based fractional vegetation cover (FVC) mapping in semi-arid vegetation. The framework combined a U-Net segmentation backbone with band-aware spectral encoding, optional lightweight cross-channel attention, NPV-weighted optimisation, data augmentation, post-inference spectral characterisation, Monte Carlo dropout-based uncertainty mapping, and edge-deployment benchmarking. Across the within-site ablation experiments, the largest gains were obtained for the difficult NPV class. M5 achieved the highest aggregate NPV F1-score of 0.496, representing a $+0.148$

improvement over the baseline M1, while M3 achieved the highest aggregate mean F1-score and mIoU, with values of 0.745 and 0.629, respectively.

The results indicate that NPV-weighted optimisation was the dominant factor improving target-class performance, while the spectral adapter and lightweight spectral transformer acted as supporting components for structuring BE–NPV–PV spectral representations. Patch scale also affected the relationship between quantitative metrics and spatial prediction quality: the larger 304 px context improved aggregate metrics, whereas the smaller 152 px configuration better preserved fine local structures during visual inference. At the sensor level, the selected MICA configuration provided stronger pixel-wise segmentation performance and finer spatial detail, whereas the selected FX10–FX17 configuration provided broader VNIR–SWIR information for interpreting spectrally ambiguous NPV, vegetation–substrate, and dry-material mixtures. Together, these sensor-specific results identify a central spatial–spectral trade-off: finer spatial resolution improved segmentation detail, whereas broader VNIR–SWIR information strengthened interpretation of spectrally ambiguous NPV and vegetation–substrate mixtures.

Post-inference spectral characterisation supported interpretation of the predicted BE, NPV, and PV classes, with NPV remaining the most uncertain and spectrally complex component. Reflectance separability, spectral-index maps, and model-derived spectral-importance rankings showed that class differences were concentrated in visible, red-edge, NIR, and selected SWIR regions consistent with greenness, pigment transition, moisture- or dry-material-sensitive variation, and substrate contribution. Monte Carlo dropout-based uncertainty mapping further showed that uncertainty was highest for NPV and concentrated around mixed vegetation–substrate transitions and heterogeneous vegetation structure. These outputs should be interpreted as diagnostic spectral and model summaries rather than direct retrievals of vegetation traits, substrate properties, or calibrated probabilities of error.

Cross-site inference provided qualitative transfer diagnostics outside the labelled training domain, while TensorRT benchmarking on Jetson AGX Orin demonstrated compatibility with embedded GPU inference, including models using high-dimensional imaging spectroscopy inputs. Overall, this study provides a lightweight, interpretable, and edge-deployable baseline for NPV-aware, sensor-informed FVC mapping in semi-arid ecosystems. Future work should extend the workflow to labelled multi-site and multi-season datasets, external validation at transfer sites, sensor-harmonised spatial–spectral ex-

periments, uncertainty calibration, and structurally or spectrally distinct ecosystems where BE–NPV–PV mixtures differ from the original training domain.

8. Acknowledgements

We would like to acknowledge the Terrestrial Ecosystem Research Network (TERN) for support, in particular the TERN Ecosystem Surveillance team and TERN Landscapes program. We would like to thank Ben Sparrow, Poornima Sivanandam and Juan Carlos Montes-Herrera for drone operation and data processing. We thank the managers of Calperum Station (Australian Landscape Trust), South Australia, for providing access to the study sites. Laura Sotomayor is supported by a Research Training Program (RTP) scholarship through the University of Tasmania. The Australian Research Council (ARC) supported some of the initial fieldwork and infrastructure under Discovery grant DP180103460. We gratefully acknowledge Prof. Megan Lewis for her valuable guidance in helping us understand semi-arid ecosystems through an integrated ecological and remote sensing perspective, and for her helpful comments on the final manuscript. We also thank all individuals who contributed to the labelling process: Prof. Megan Lewis (School of Biological Sciences, University of Adelaide), Dr Krishna Lamsal (School of Geography, Planning, and Spatial Sciences, UTAS), Dr. Agustina Barros (Researcher at National Scientific and Technical Research Council), Dr. Sebastian Rossi (Researcher at National Scientific and Technical Research Council), Molly Marshall (School of Geography, Planning, and Spatial Sciences, UTAS) and Sophia Hoyer (School of Geography, Planning, and Spatial Sciences, UTAS). The authors gratefully acknowledge NVIDIA for selecting the project *Mapping Ecosystem Resilience with High-Resolution Remote Sensing Data* for inclusion in the NVIDIA Academic Grant Program. This six-month award provided cloud access through Brev to one reserved instance of 8× NVIDIA A100 80 GB GPUs from October 1, 2025 to March 31, 2026, comprising 80 GiB VRAM per GPU, 2 TiB RAM, 128 CPUs, 60 TiB of storage, and 560 GiB NVMe storage. Multiple team members were permitted to use the resource, although only one instance was allocated to the project. The authors also gratefully acknowledge NVIDIA AI Technology for the research collaboration and additional computational support provided during model development and testing. These resources included a Brev/SFCompute NVIDIA H100 environment with 8× NVIDIA H100 GPUs,

74 GiB available GPU memory per GPU, 112 CPUs, 894 GiB RAM, and 1.36 TiB storage, together with an NVIDIA Jetson AGX Orin 32 GB device with 12 CPU cores, 30 GB available RAM, and 298 GB storage for edge-compute testing.

Appendix A. Additional within-site performance diagnostics

This appendix reports additional within-site performance diagnostics that complement the main results. These include NPV intersection-over-union (IoU), macro-averaged mean F1-score, the NPV F1–mIoU trade-off, and class-wise F1-score and IoU for bare ground (BE), non-photosynthetic vegetation (NPV), and photosynthetic vegetation (PV). These diagnostics support interpretation of the aggregate performance summary by showing whether improvements in NPV F1, mean F1, and mIoU were associated with class-specific gains or trade-offs across sensor profiles, patch scales, and model variants.

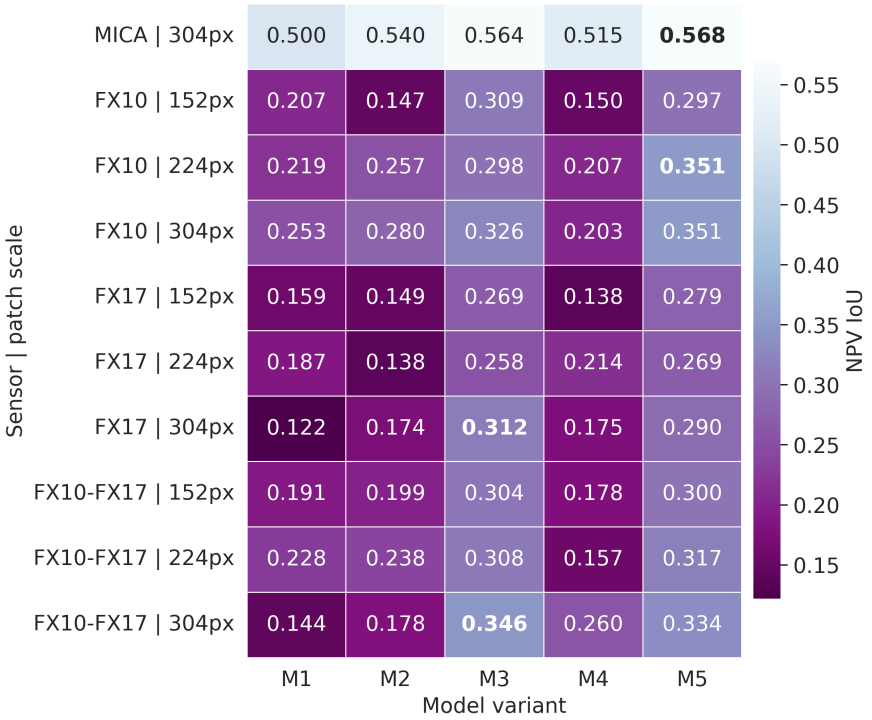

Figure Appendix A.1: Additional within-site target-class performance across model variants, sensor profiles, and patch scales. Values show NPV intersection-over-union (IoU) for each sensor-profile and patch-scale configuration. Rows denote sensor-profile and patch-scale combinations, and columns denote model variants M1–M5. Bold values indicate the best-performing variant within each sensor row. The heatmap complements the NPV F1-score results reported in the main text by showing the corresponding overlap-based target-class performance.

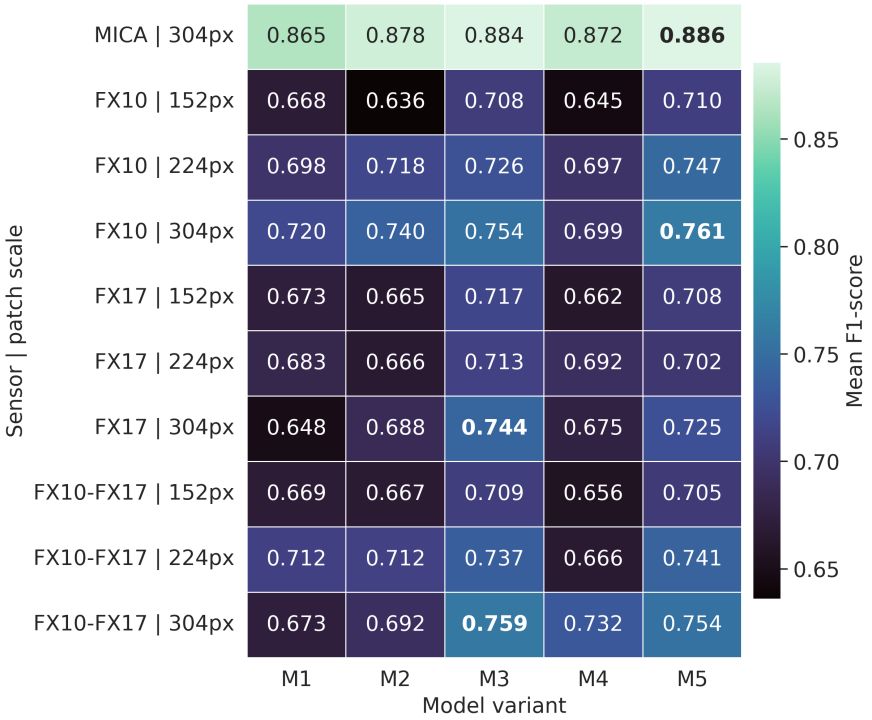

Figure Appendix A.2: Additional within-site aggregate segmentation performance across model variants, sensor profiles, and patch scales. Values show macro-averaged mean F1-score across bare ground (BE), non-photosynthetic vegetation (NPV), and photosynthetic vegetation (PV). Rows denote sensor-profile and patch-scale combinations, and columns denote model variants M1–M5. Bold values indicate the best-performing variant within each sensor row. The heatmap complements the mIoU results reported in the main text by showing the corresponding F1-based aggregate segmentation performance.

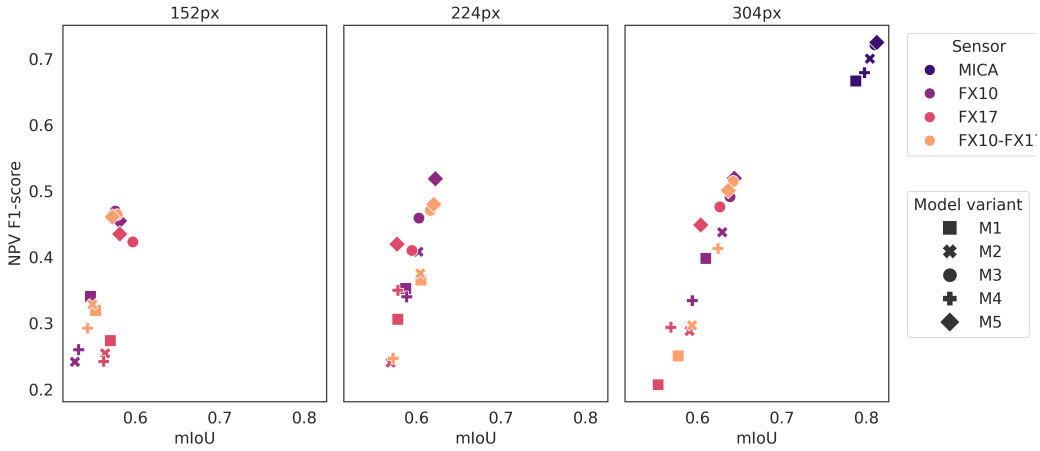

Figure Appendix A.3: Within-site trade-off between target-class NPV F1-score and aggregate mIoU across patch scales. Each panel corresponds to a patch scale, with points representing individual sensor-profile and model-variant combinations. The x-axis shows mIoU computed across BE, NPV, and PV, while the y-axis shows NPV F1-score. Colours denote sensor profiles and marker shapes denote model variants M1–M5. Points in the upper-right region indicate configurations that jointly improve NPV detection and overall segmentation quality. The plot complements the heatmap summaries by showing that the NPV-weighted variants generally shift configurations toward higher NPV F1-score while maintaining comparable or improved mIoU.

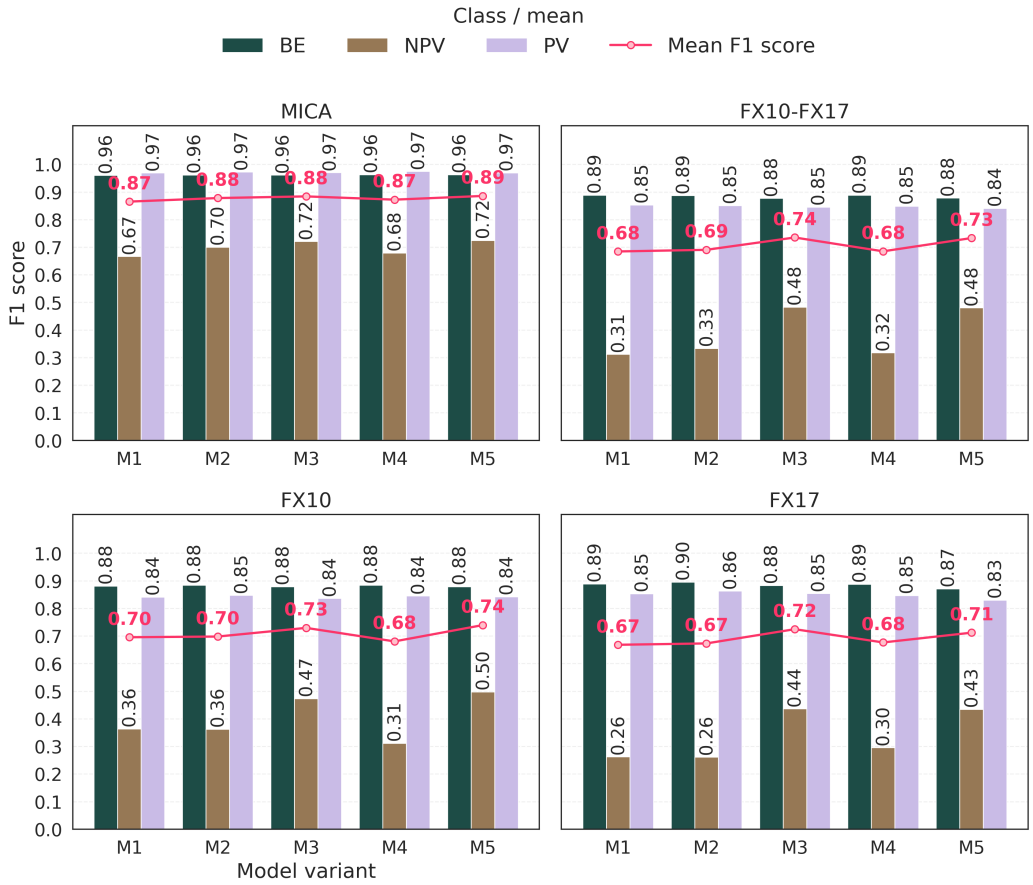

Figure Appendix A.4: Class-wise within-site F1-score across sensor profiles and model variants. Panels show the MICA, FX10–FX17, FX10, and FX17 sensor profiles, with model variants M1–M5 shown on the x-axis. Bars indicate class-wise F1-score for bare ground (BE), non-photosynthetic vegetation (NPV), and photosynthetic vegetation (PV), using a consistent class palette across panels. The line indicates the macro-averaged mean F1-score across the three FVC classes for each model variant. M1 is the baseline U-Net, M2 is the spectral-adapter CNN, M3 is the NPV-weighted spectral-adapter CNN, M4 is the spectral-adapter CNN with the lightweight spectral transformer, and M5 is the NPV-weighted spectral-adapter CNN with the lightweight spectral transformer. The figure highlights that BE and PV achieved consistently high F1-scores across sensor profiles, whereas NPV remained the limiting class. The NPV-weighted variants, particularly M3 and M5, improved NPV F1-score most clearly for the hyperspectral sensor profiles while maintaining high BE and PV performance.

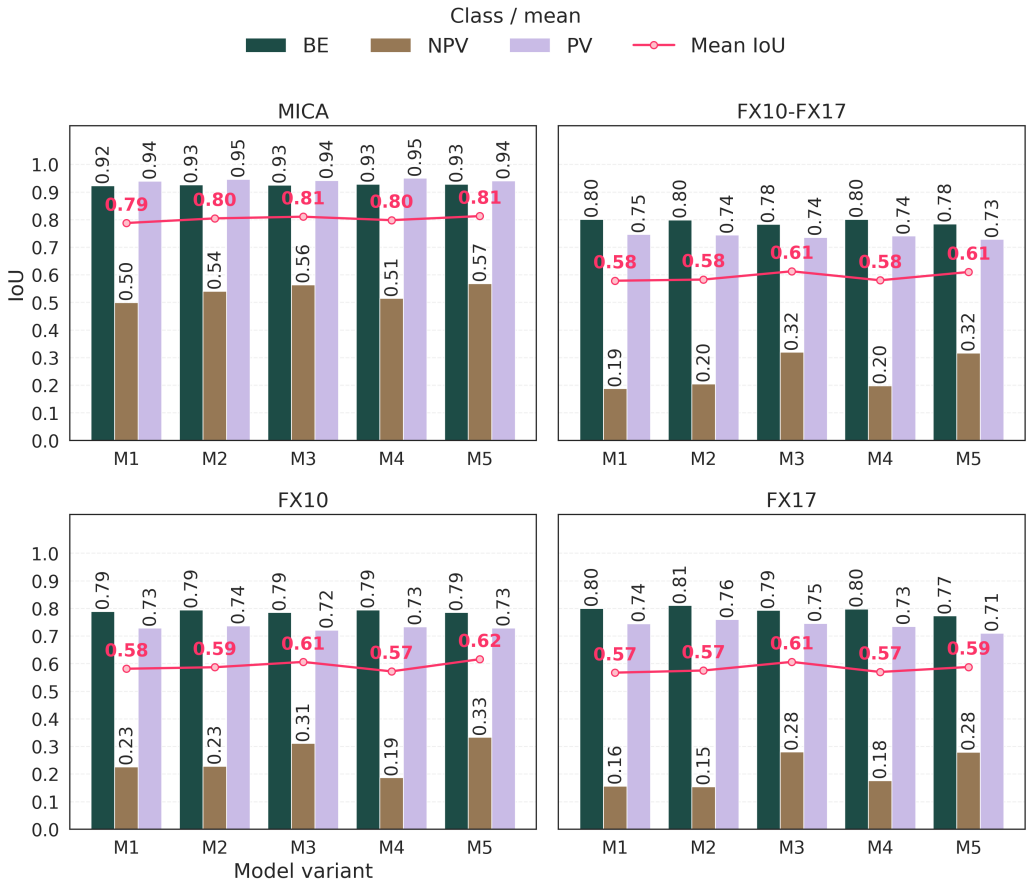

Figure Appendix A.5: Class-wise within-site intersection-over-union (IoU) across sensor profiles and model variants. Panels show the MICA, FX10–FX17, FX10, and FX17 sensor profiles, with model variants M1–M5 shown on the x-axis. Bars indicate class-wise IoU for bare ground (BE), non-photosynthetic vegetation (NPV), and photosynthetic vegetation (PV), using the same class palette as the class-wise F1-score figure. The line indicates the macro-averaged mean IoU across the three FVC classes for each model variant. M1 is the baseline U-Net, M2 is the spectral-adapter CNN, M3 is the NPV-weighted spectral-adapter CNN, M4 is the spectral-adapter CNN with the lightweight spectral transformer, and M5 is the NPV-weighted spectral-adapter CNN with the lightweight spectral transformer. The IoU results show the same class-level pattern as the F1-score results, with high BE and PV overlap and substantially lower NPV overlap. Improvements in mean IoU were therefore mainly controlled by gains in NPV, especially for the NPV-weighted variants M3 and M5.

Appendix B. Supplementary deployment diagnostics

This appendix provides additional diagnostic information supporting the TensorRT deployment results reported in Section 5.3. The supplementary material includes ONNX export metadata, full parity diagnostics, latency-throughput behaviour, and representative tile-level parity maps relative to the PyTorch reference.

Appendix B.1. ONNX export metadata

The selected FX10–FX17 s152 and MICA s304 segmentation models were exported to ONNX before TensorRT engine construction. Table Appendix B.1 summarises the exported model interfaces. Both exports used dynamic batch and spatial dimensions and produced three-channel logits corresponding to BE, NPV, and PV.

Table Appendix B.1: Supplementary ONNX export metadata for the selected deployment models.

Sensor	Input tensor	Output tensor	Nodes	Weights (MB)
FX10–FX17 s152	FLOAT[batch, 296, height, width]	FLOAT[batch, 3, height, width]	218	125.47
MICA s304	FLOAT[batch, 10, height, width]	FLOAT[batch, 3, height, width]	213	126.53

Appendix B.2. Full parity diagnostics

Table Appendix B.2 reports logit-level and argmax-level parity relative to the PyTorch reference. ONNX Runtime reproduced the PyTorch outputs exactly within the reported precision for both sensors. TensorRT FP32 preserved near-identical predictions, while the validated FP16-labelled engines showed larger logit differences but maintained high argmax agreement. Pure FP16 TensorRT engines are not tabulated because they produced non-finite logits and were excluded from deployment interpretation.

Table Appendix B.2: Supplementary parity diagnostics relative to the PyTorch reference. Agreement and mIoU were computed from argmax predictions relative to PyTorch. FP16-labelled rows correspond to validated mixed FP16/FP32 TensorRT engines rather than pure FP16 engines.

Sensor	**Backend**	**max $\lvert\Delta\rvert$**	**$\overline{\lvert\Delta\rvert}$**	**Agree (%)**	**mIoU**
FX10–FX17 s152	ONNX Runtime	0.00	0.00	100.0000	1.0000
FX10–FX17 s152	TRT FP32	5.62×10^{-5}	5.04×10^{-6}	100.0000	1.0000
FX10–FX17 s152	TRT FP16	1.80×10^{-2}	1.50×10^{-3}	99.9636	0.9991
MICA s304	ONNX Runtime	0.00	0.00	100.0000	1.0000
MICA s304	TRT FP32	1.73×10^{-3}	6.05×10^{-5}	99.9987	1.0000
MICA s304	TRT FP16	1.23×10^{-2}	4.20×10^{-4}	99.9933	0.9998

Appendix B.3. TensorRT latency-throughput diagnostic

The main text reports the deployment-ready TensorRT configurations in Table 11 and summarises the speed–parity trade-off in Figure 12. Figure Appendix B.1 provides the corresponding latency-throughput diagnostic.

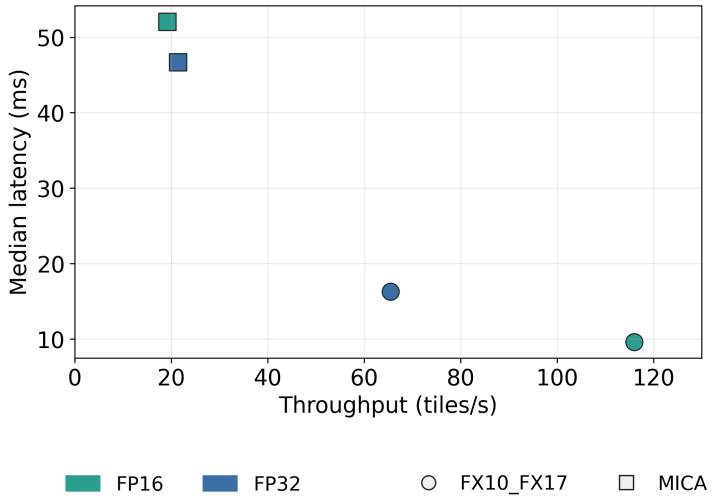

Figure Appendix B.1: Supplementary TensorRT latency-throughput diagnostic on Jetson AGX Orin. The x-axis shows throughput in tiles s^{-1}, and the y-axis shows median per-tile latency in milliseconds. Points farther to the lower-right indicate higher-throughput and lower-latency deployment configurations. FP16-labelled points correspond to validated mixed FP16/FP32 TensorRT engines obtained after Polygraphy precision debugging.

Appendix B.4. TensorRT parity maps

Representative tile-level parity maps are shown for the deployment-ready TensorRT FP32 engines and the validated FP16-labelled mixed FP16/FP32

engines. Pure FP16 TensorRT engines and intermediate precision-debugging configurations are omitted because they were not deployment-ready.

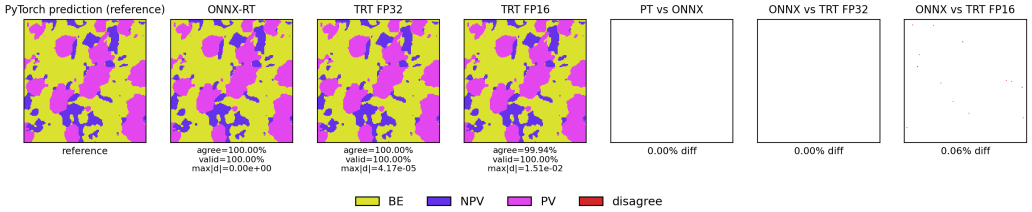

(a) FX10–FX17 s152

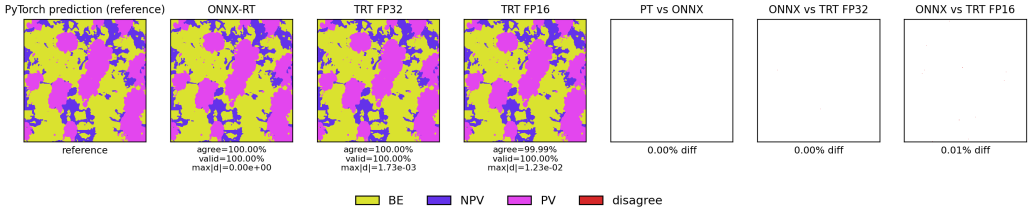

(b) MICA s304

Figure Appendix B.2: Supplementary TensorRT parity maps for representative FX10–FX17 s152 and MICA s304 inference tiles. PyTorch predictions are used as the reference and compared with deployment-ready TensorRT FP32 and FP16-labelled mixed FP16/FP32 outputs. Class-map panels show BE, NPV, and PV predictions, while disagreement panels highlight pixel-wise differences relative to the PyTorch reference. White indicates agreement and red indicates disagreement.

Code and Data Availability

The full FVC mapping workflow developed in this study, *hyperFVC*, is available at `https://github.com/LNSOTOM/fvc_function`. The repository contains the code structure for multi-sensor UAS FVC segmentation, spectral-encoding model variants, post-inference spectral characterisation, and edge-deployment benchmarking. The version used in this manuscript is 2026.28.4. Code required to reproduce the final experiments and results will be made publicly available after acceptance of the manuscript.

The UAS imagery, tiled datasets, and manual FVC reference labels used in this study are available from Zenodo at `https://zenodo.org/records/15036860`.

Declaration of generative AI and AI-assisted technologies in the manuscript preparation process.

During the preparation of this work the author(s) used ChatGPT for language editing. During analysis, the authors employed GitHub Copilot for programming assistance. After using these tools, the author(s) reviewed and edited the content and code as needed and take(s) full responsibility for the content of the published article and code.

References

Asner, G.P., Martin, R.E., 2009. Airborne spectranomics: mapping canopy chemical and taxonomic diversity in tropical forests. Frontiers in Ecology and the Environment 7, 269–276. URL: https://onlinelibrary.wiley.com/doi/abs/10.1890/070152, doi:10.1890/070152. _eprint: https://esajournals.onlinelibrary.wiley.com/doi/pdf/10.1890/070152.

Bian, J., Li, A., Zhang, Z., Zhao, W., Lei, G., Xia, H., Tan, J., 2016. Grassland fractional vegetation cover monitoring using the composited HJ-1A/B time series images and unmanned aerial vehicles: A case study in Zoige wetland, China, in: 2016 IEEE International Geoscience and Remote Sensing Symposium (IGARSS), pp. 7192–7195. URL: https://ieeexplore.ieee.org/document/7730876, doi:10.1109/IGARSS.2016.7730876.

Bollard, B., Doshi, A., Gilbert, N., Poirot, C., Gillman, L., 2022. Drone Technology for Monitoring Protected Areas in Remote and Fragile Environments. Drones 6, 42. URL: https://www.mdpi.com/2504-446X/6/2/42, doi:10.3390/drones6020042. publisher: Multidisciplinary Digital Publishing Institute.

Braham, N.A.A., Albrecht, C.M., Mairal, J., Chanussot, J., Wang, Y., Zhu, X.X., 2025. SpectralEarth: Training Hyperspectral Foundation Models at Scale. IEEE Journal of Selected Topics in Applied Earth Observations and Remote Sensing 18, 16780–16797. URL: https://ieeexplore.ieee.org/document/11045062, doi:10.1109/JSTARS.2025.3581451.

Brodribb, T., Brodersen, C.R., Carriqui, M., Tonet, V., Rodriguez Dominguez, C., McAdam, S., 2021. Linking xylem network failure with leaf tissue death. New Phytologist 232, 68–79. URL: https://onlinelibrary.wiley.com/doi/abs/10.1111/nph.17577, doi:10.1111/

nph.17577. tex.copyright: © 2021 The Authors. New Phytologist © 2021 New Phytologist Foundation.

Brodribb, T.J., Powers, J., Cochard, H., Choat, B., 2020. Hanging by a thread? Forests and drought. Science 368, 261–266. URL: https://www.science.org/doi/full/10.1126/science.aat7631, doi:10.1126/science.aat7631.

Brodrick, P.G., Davies, A.B., Asner, G.P., 2019. Uncovering Ecological Patterns with Convolutional Neural Networks. Trends in Ecology & Evolution 34, 734–745. URL: https://www.sciencedirect.com/science/article/pii/S0169534719300862, doi:10.1016/j.tree.2019.03.006.

Chabrillat, S., Foerster, S., Segl, K., Beamish, A., Brell, M., Asadzadeh, S., Milewski, R., Ward, K.J., Brosinsky, A., Koch, K., Scheffler, D., Guillaso, S., Kokhanovsky, A., Roessner, S., Guanter, L., Kaufmann, H., Pinnel, N., Carmona, E., Storch, T., Hank, T., Berger, K., Wocher, M., Hostert, P., van der Linden, S., Okujeni, A., Janz, A., Jakimow, B., Bracher, A., Soppa, M.A., Alvarado, L.M.A., Buddenbaum, H., Heim, B., Heiden, U., Moreno, J., Ong, C., Bohn, N., Green, R.O., Bachmann, M., Kokaly, R., Schodlok, M., Painter, T.H., Gascon, F., Buongiorno, F., Mottus, M., Brando, V.E., Feilhauer, H., Betz, M., Baur, S., Feckl, R., Schickling, A., Krieger, V., Bock, M., La Porta, L., Fischer, S., 2024. The EnMAP spaceborne imaging spectroscopy mission: Initial scientific results two years after launch. Remote Sensing of Environment 315, 114379. URL: https://www.sciencedirect.com/science/article/pii/S003442572400405X, doi:10.1016/j.rse.2024.114379.

Chen, J., Yi, S., Qin, Y., Wang, X., 2016. Improving estimates of fractional vegetation cover based on UAV in alpine grassland on the Qinghai–Tibetan Plateau. International Journal of Remote Sensing 37, 1922–1936. URL: https://doi.org/10.1080/01431161.2016.1165884, doi:10.1080/01431161.2016.1165884.

Cherif, E., Feilhauer, H., Berger, K., Dao, P.D., Ewald, M., Hank, T.B., He, Y., Kovach, K.R., Lu, B., Townsend, P.A., Kattenborn, T., 2023. From spectra to plant functional traits: Transferable multi-trait models from heterogeneous and sparse data. Remote Sensing of Environment 292, 113580. URL: https://www.sciencedirect.com/science/article/pii/S0034425723001311, doi:10.1016/j.rse.2023.113580.

Choi, S.K., Lee, S.K., Jung, S.H., Choi, J.W., Choi, D.Y., Chun, S.J., 2016. Estimation of Fractional Vegetation Cover in Sand Dunes Using Multi-spectral Images from Fixed-wing UAV. Journal of the Korean Society of Surveying, Geodesy, Photogrammetry and Cartography 34, 431–441. URL: https://koreascience.or.kr/article/JAKO201625752509115.page, doi:10.7848/ksgpc.2016.34.4.431.

Chowdhury, A.I., Beloiu, M., Kattenborn, T., Mosig, C., Ahishali, M., Vastaranta, M., Puttonen, E., Honkavaara, E., Huo, L., Uddin, M.J., Griess, V.C., Kuzmin, A., Cheng, Y., Junttila, S., 2026. Remote sensing and deep learning for standing dead-tree detection and mapping: A review of advances, challenges, and future directions URL: https://eartharxiv.org/repository/view/12931/. publisher: EarthArXiv.

Cimoli, E., Lucieer, A., Malenovský, Z., Woodgate, W., Janoutová, R., Turner, D., Haynes, R.S., Phinn, S., 2024. Mapping functional diversity of canopy physiological traits using UAS imaging spectroscopy. Remote Sensing of Environment 302, 113958. URL: https://www.sciencedirect.com/science/article/pii/S0034425723005102, doi:10.1016/j.rse.2023.113958.

Cimoli, E., Lucieer, V., Meiners, K.M., Chennu, A., Castrisios, K., Ryan, K.G., Lund-Hansen, L.C., Martin, A., Kennedy, F., Lucieer, A., 2020. Mapping the in situ microspatial distribution of ice algal biomass through hyperspectral imaging of sea-ice cores. Scientific Reports 10, 21848. URL: https://www.nature.com/articles/s41598-020-79084-6, doi:10.1038/s41598-020-79084-6. tex.copyright: 2020 The Author(s).

Cimoli, E., Montes-Herrera, J.C., Cummings, V., Marriott, P., Haynes, R.S., 2026. Advancing Monitoring of Nearshore Antarctic Sea Ice and Benthic Ecosystems with HIcyBot. Oceanography 39, 6–13. URL: https://tos.org/oceanography/article/advancing-monitoring-of-nearshore-antarctic-sea-ice-and-benthic-ecosystems-with doi:10.5670/oceanog.2026.e107.

Cotrozzi, L., 2022. Spectroscopic detection of forest diseases: a review (1970–2020). Journal of Forestry Research 33, 21–38. URL: https://doi.org/10.1007/s11676-021-01378-w, doi:10.1007/s11676-021-01378-w.

DCCEEW, 2017. Australian Vegetation Attribute Manual Version 7.0 - DCCEEW. URL: https://www.dcceew.gov.au/environment/land/publications/australian-vegetation-attribute-manual-version-7.

Dou, H., Lin, T., Xu, Q., Wang, J., Xu, H., Aili, A., Zhang, P., Wang, C., Zhao, W., 2025. Ecohydrological significance of microtopography in arid Zones: Regulating Water, supporting Vegetation, promoting ecosystem stability. Ecological Indicators 171, 113200. URL: https://www.sciencedirect.com/science/article/pii/S1470160X25001293, doi:10.1016/j.ecolind.2025.113200.

Fisk, C., Clarke, K.D., Delean, S., Lewis, M.M., 2019a. Distinguishing Photosynthetic and Non-Photosynthetic Vegetation: How Do Traditional Observations and Spectral Classification Compare? Remote Sensing 11, 2589. URL: https://www.mdpi.com/2072-4292/11/21/2589, doi:10.3390/rs11212589.

Fisk, C., Clarke, K.D., Lewis, M.M., 2019b. Comparison of Hyperspectral Versus Traditional Field Measurements of Fractional Ground Cover in the Australian Arid Zone. Remote Sensing 11, 2825. URL: https://www.mdpi.com/2072-4292/11/23/2825, doi:10.3390/rs11232825. number: 23 Publisher: Multidisciplinary Digital Publishing Institute.

Gal, Y., Ghahramani, Z., 2016. Dropout as a Bayesian Approximation: Representing Model Uncertainty in Deep Learning. URL: http://arxiv.org/abs/1506.02142, doi:10.48550/arXiv.1506.02142.

Guanter, L., Kaufmann, H., Segl, K., Foerster, S., Rogass, C., Chabrillat, S., Kuester, T., Hollstein, A., Rossner, G., Chlebek, C., Straif, C., Fischer, S., Schrader, S., Storch, T., Heiden, U., Mueller, A., Bachmann, M., Mühle, H., Müller, R., Habermeyer, M., Ohndorf, A., Hill, J., Buddenbaum, H., Hostert, P., Van der Linden, S., Leitão, P.J., Rabe, A., Doerffer, R., Krasemann, H., Xi, H., Mauser, W., Hank, T., Locherer, M., Rast, M., Staenz, K., Sang, B., 2015. The EnMAP Spaceborne Imaging Spectroscopy Mission for Earth Observation. Remote Sensing 7, 8830–8857. URL: https://www.mdpi.com/2072-4292/7/7/8830, doi:10.3390/rs70708830.

Harrison, B.A., Gibson, R., Bastin, G., Thackway, R., Huete, A., Donald, G., Lyons, M., Sparks, T., Byrne, G., Lewis, M.M., Xie, Q., 2021. Earth Observation: Data, Processing and Applications. Volume 3A: Applications—Terrestrial Vegetation. Australia and New Zealand CRC for Spatial Information. URL: https://opus.lib.uts.edu.au/handle/10453/155085. tex.copyright: info:eu-repo/semantics/openAccess.

Haut, J.M., Bernabé, S., Paoletti, M.E., Fernandez-Beltran, R., Plaza, A., Plaza, J., 2019. Low–High-Power Consumption Architectures for Deep-Learning Models Applied to Hyperspectral Image Classification. IEEE Geoscience and Remote Sensing Letters 16, 776–780. URL: https://ieeexplore.ieee.org/abstract/document/8554064, doi:10.1109/LGRS.2018.2881045.

Haynes, R.S., Lucieer, A., Brodribb, T.J., Tonet, V., Cimoli, E., 2024. Predicting key water stress indicators of Eucalyptus viminalis and Callitris rhomboidea using high-resolution visible to short-wave infrared spectroscopy. Plant, Cell & Environment 47, 4992–5006. URL: https://onlinelibrary.wiley.com/doi/abs/10.1111/pce.15083, doi:10.1111/pce.15083. tex.copyright: © 2024 The Author(s). Plant, Cell & Environment published by John Wiley & Sons Ltd.

Haynes, R.S., Lucieer, A., Turner, D., Cimoli, E., 2025. Co-Registration of Multi-Modal UAS Pushbroom Imaging Spectroscopy and RGB Imagery Using Optical Flow. Drones 9, 132. URL: https://www.mdpi.com/2504-446X/9/2/132, doi:10.3390/drones9020132.

Haynes, R.S., Lucieer, A., Turner, D., Cimoli, E., Sivanandam, P., Brodribb, T.J., 2026. UAS ecophysiology: Imaging spectroscopy can map canopy leaf water potential in a diverse forest ecosystem. Remote Sensing of Environment 344, 115532. URL: https://www.sciencedirect.com/science/article/pii/S0034425726003020, doi:10.1016/j.rse.2026.115532.

He, X., Chen, Y., Lin, Z., 2021. Spatial-Spectral Transformer for Hyperspectral Image Classification. Remote Sensing 13, 498. URL: https://www.mdpi.com/2072-4292/13/3/498, doi:10.3390/rs13030498. publisher: Multidisciplinary Digital Publishing Institute.

Hendrycks, D., Gimpel, K., 2023. Gaussian Error Linear Units (GELUs).

URL: http://arxiv.org/abs/1606.08415, doi:10.48550/arXiv.1606.08415. arXiv:1606.08415 [cs.LG].

Homolová, L., Malenovský, Z., Clevers, J.G.P.W., García-Santos, G., Schaepman, M.E., 2013. Review of optical-based remote sensing for plant trait mapping. Ecological Complexity 15, 1–16. URL: https://www.sciencedirect.com/science/article/pii/S1476945X13000524, doi:10.1016/j.ecocom.2013.06.003.

Hong, D., Han, Z., Yao, J., Gao, L., Zhang, B., Plaza, A., Chanussot, J., 2022. SpectralFormer: Rethinking Hyperspectral Image Classification with Transformers. IEEE Transactions on Geoscience and Remote Sensing 60, 1–15. URL: http://arxiv.org/abs/2107.02988, doi:10.1109/TGRS.2021.3130716. arXiv:2107.02988 [cs.CV].

Hu, J., Shen, L., Albanie, S., Sun, G., Wu, E., 2019. Squeeze-and-Excitation Networks. URL: http://arxiv.org/abs/1709.01507, doi:10.48550/arXiv.1709.01507. arXiv:1709.01507 [cs.CV].

Huang, B., Lu, K., Audeberr, N., Khalel, A., Tarabalka, Y., Malof, J., Boulch, A., Le Saux, B., Collins, L., Bradbury, K., Lefèvre, S., El-Saban, M., 2018. Large-Scale Semantic Classification: Outcome of the First Year of Inria Aerial Image Labeling Benchmark, in: IGARSS 2018 - 2018 IEEE International Geoscience and Remote Sensing Symposium, pp. 6947–6950. URL: https://ieeexplore.ieee.org/document/8518525, doi:10.1109/IGARSS.2018.8518525. iSSN: 2153-7003.

Hurtado, J.V., Mohan, R., Valada, A., 2025. Hyperspectral Adapter for Semantic Segmentation with Vision Foundation Models. URL: http://arxiv.org/abs/2509.20107, doi:10.48550/arXiv.2509.20107. arXiv:2509.20107 [cs.CV].

Jiang, X., Wu, Z., Han, S., Yan, H., Zhou, B., Li, J., 2023. A multi-scale approach to detecting standing dead trees in UAV RGB images based on improved faster R-CNN. PLOS ONE 18, e0281084. URL: https://journals.plos.org/plosone/article?id=10.1371/journal.pone.0281084, doi:10.1371/journal.pone.0281084. publisher: Public Library of Science.

Joshi, D., Witharana, C., 2025. Vision Transformer-Based Unhealthy Tree Crown Detection in Mixed Northeastern US Forests and Evaluation of Annotation Uncertainty. Remote Sensing 17, 1066. URL: https://www.mdpi.com/2072-4292/17/6/1066, doi:10.3390/rs17061066. publisher: Multidisciplinary Digital Publishing Institute.

Jutras-Perreault, M.C., Næsset, E., Gobakken, T., Ørka, H.O., 2023. Detecting the presence of standing dead trees using airborne laser scanning and optical data. Scandinavian Journal of Forest Research 38, 208–220. URL: https://doi.org/10.1080/02827581.2023.2211807, doi:10.1080/02827581.2023.2211807. publisher: Taylor & Francis _eprint: https://doi.org/10.1080/02827581.2023.2211807.

Kattenborn, T., Eichel, J., Fassnacht, F.E., 2019a. Convolutional Neural Networks enable efficient, accurate and fine-grained segmentation of plant species and communities from high-resolution UAV imagery. Scientific Reports 9, 17656. doi:10.1038/s41598-019-53797-9.

Kattenborn, T., Eichel, J., Wiser, S., Burrows, L., Fassnacht, F.E., Schmidtlein, S., 2020. Convolutional Neural Networks accurately predict cover fractions of plant species and communities in Unmanned Aerial Vehicle imagery. Remote Sensing in Ecology and Conservation 6, 472–486. URL: https://onlinelibrary.wiley.com/doi/10.1002/rse2.146, doi:10.1002/rse2.146.

Kattenborn, T., Fassnacht, F.E., Schmidtlein, S., 2019b. Differentiating plant functional types using reflectance: which traits make the difference? Remote Sensing in Ecology and Conservation 5, 5–19. URL: https://zslpublications.onlinelibrary.wiley.com/doi/10.1002/rse2.86, doi:10.1002/rse2.86. publisher: John Wiley & Sons, Ltd.

Kattenborn, T., Leitloff, J., Schiefer, F., Hinz, S., 2021. Review on Convolutional Neural Networks (CNN) in vegetation remote sensing. ISPRS Journal of Photogrammetry and Remote Sensing 173, 24–49. URL: https://www.sciencedirect.com/science/article/pii/S0924271620303488, doi:10.1016/j.isprsjprs.2020.12.010.

Kattenborn, T., Schiefer, F., Frey, J., Feilhauer, H., Mahecha, M.D., Dormann, C.F., 2022. Spatially autocorrelated training and valida-

tion samples inflate performance assessment of convolutional neural networks. ISPRS Open Journal of Photogrammetry and Remote Sensing 5, 100018. URL: https://www.sciencedirect.com/science/article/pii/S2667393222000072, doi:10.1016/j.ophoto.2022.100018.

Kattenborn, T., Schiefer, F., Zarco-Tejada, P., Schmidtlein, S., 2019c. Advantages of retrieving pigment content [g/cm2] versus concentration [%] from canopy reflectance. Remote Sensing of Environment 230, 111195. URL: https://www.sciencedirect.com/science/article/pii/S003442571930207X, doi:10.1016/j.rse.2019.05.014.

Kattenborn, T., Wieneke, S., Montero, D., Mahecha, M.D., Richter, R., Guimarães-Steinicke, C., Wirth, C., Ferlian, O., Feilhauer, H., Sachsenmaier, L., Eisenhauer, N., Dechant, B., 2024. Temporal dynamics in vertical leaf angles can confound vegetation indices widely used in Earth observations. Communications Earth & Environment 5, 550. URL: https://www.nature.com/articles/s43247-024-01712-0, doi:10.1038/s43247-024-01712-0. tex.copyright: 2024 The Author(s).

Koubaa, A., Ammar, A., Abdelkader, M., Alhabashi, Y., Ghouti, L., 2023. AERO: AI-Enabled Remote Sensing Observation with Onboard Edge Computing in UAVs. Remote Sensing 15, 1873. URL: https://www.mdpi.com/2072-4292/15/7/1873, doi:10.3390/rs15071873. publisher: Multidisciplinary Digital Publishing Institute.

Lewis, M., Jooste, V., de Gasparis, A., 2001. Discrimination of arid vegetation with airborne multispectral scanner hyperspectral imagery. IEEE Transactions on Geoscience and Remote Sensing 39, 1471–1479. URL: https://ieeexplore.ieee.org/abstract/document/934078, doi:10.1109/36.934078.

Li, L., Mu, X., Jiang, H., Chianucci, F., Hu, R., Song, W., Qi, J., Liu, S., Zhou, J., Chen, L., Huang, H., Yan, G., 2023. Review of ground and aerial methods for vegetation cover fraction (fCover) and related quantities estimation: definitions, advances, challenges, and future perspectives. ISPRS Journal of Photogrammetry and Remote Sensing 199, 133–156. URL: https://www.sciencedirect.com/science/article/pii/S0924271623000801, doi:10.1016/j.isprsjprs.2023.03.020.

Li, Y., Luo, Y., Zhang, L., Wang, Z., Du, B., 2024. MambaHSI: Spatial–Spectral Mamba for Hyperspectral Image Classification. IEEE Transactions on Geoscience and Remote Sensing 62, 1–16. URL: https://ieeexplore.ieee.org/abstract/document/10604894, doi:10.1109/TGRS.2024.3430985.

Lin, M., Chen, Q., Yan, S., 2014. Network In Network. URL: http://arxiv.org/abs/1312.4400, doi:10.48550/arXiv.1312.4400. arXiv:1312.4400 [cs.NE].

Lin, T.Y., Goyal, P., Girshick, R., He, K., Dollár, P., 2017. Focal Loss for Dense Object Detection. URL: https://ui.adsabs.harvard.edu/abs/2017arXiv170802002L, doi:10.48550/arXiv.1708.02002.

Liu, J., Xiang, J., Jin, Y., Liu, R., Yan, J., Wang, L., 2021. Boost Precision Agriculture with Unmanned Aerial Vehicle Remote Sensing and Edge Intelligence: A Survey. Remote Sensing 13, 4387. URL: https://www.mdpi.com/2072-4292/13/21/4387, doi:10.3390/rs13214387. publisher: Multidisciplinary Digital Publishing Institute.

Lucieer, A., Turner, D., King, D.H., Robinson, S.A., 2014. Using an Unmanned Aerial Vehicle (UAV) to capture micro-topography of Antarctic moss beds. International Journal of Applied Earth Observation and Geoinformation 27, 53–62. doi:10.1016/j.jag.2013.05.011.

López-Fandiño, J., B. Heras, D., Argüello, F., 2024. Using heterogeneous computing and edge computing to accelerate anomaly detection in remotely sensed multispectral images. The Journal of Supercomputing 80, 12543–12563. URL: https://doi.org/10.1007/s11227-024-05918-z, doi:10.1007/s11227-024-05918-z.

Makarov, A., Mirpulatov, I., Firsov, N., Lobanov, V., Illarionova, S., Podlipnov, V., Vybornova, Y., Shadrin, D., Rastorguev, A., Skidanov, R., Burnaev, E., Nikonorov, A., 2025. Deep Spectral-Spatial Transformer for Robust Hyperspectral Image Segmentation in Varying Field Conditions. IEEE Access 13, 97454–97471. URL: https://ieeexplore.ieee.org/document/11021539, doi:10.1109/ACCESS.2025.3575699.

Malenovský, Z., Lucieer, A., King, D.H., Turnbull, J.D., Robinson, S.A., 2017. Unmanned aircraft system advances health mapping of fragile polar

vegetation. Methods in Ecology and Evolution 8, 1842–1857. URL: https://onlinelibrary.wiley.com/doi/10.1111/2041-210X.12833, doi:10.1111/2041-210X.12833.

Malenovský, Z., Turnbull, J.D., Lucieer, A., Robinson, S.A., 2015. Antarctic moss stress assessment based on chlorophyll content and leaf density retrieved from imaging spectroscopy data. New Phytologist 208, 608–624. URL: https://onlinelibrary.wiley.com/doi/abs/10.1111/nph.13524, doi:10.1111/nph.13524. tex.copyright: © 2015 The Authors New Phytologist © 2015 New Phytologist Trust.

Melville, B., Fisher, A., Lucieer, A., 2019a. Ultra-high spatial resolution fractional vegetation cover from unmanned aerial multispectral imagery. International Journal of Applied Earth Observation and Geoinformation 78, 14–24. URL: https://www.sciencedirect.com/science/article/pii/S0303243418311693, doi:10.1016/j.jag.2019.01.013.

Melville, B., Fisher, A., Lucieer, A., 2019b. Ultra-high spatial resolution fractional vegetation cover from unmanned aerial multispectral imagery. International Journal of Applied Earth Observation and Geoinformation 78, 14–24. doi:10.1016/j.jag.2019.01.013.

Merton, R., 1998. Monitoring community hysteresis using spectral shift analysis and the red-edge vegetation stress index, in: Proceedings of the Seventh Annual JPL Airborne Earth Science Workshop, JPL Pasadena, CA, USA. pp. 12–16. URL: https://aviris.jpl.nasa.gov/proceedings/workshops/98_docs/37.pdf.

Mittal, S., 2019. A Survey on optimized implementation of deep learning models on the NVIDIA Jetson platform. Journal of Systems Architecture 97, 428–442. URL: https://www.sciencedirect.com/science/article/pii/S1383762118306404, doi:10.1016/j.sysarc.2019.01.011.

Montero, D., Aybar, C., Mahecha, M.D., Martinuzzi, F., Söchting, M., Wieneke, S., 2023. A standardized catalogue of spectral indices to advance the use of remote sensing in Earth system research. Scientific Data 10, 197. URL: https://www.nature.com/articles/s41597-023-02096-0, doi:10.1038/s41597-023-02096-0. tex.copyright: 2023 The Author(s).

Montes-Herrera, J.C., Cimoli, E., Cummings, V.J., D'Archino, R., Nelson, W.A., Lucieer, A., Lucieer, V., 2024. Quantifying pigment content in crustose coralline algae using hyperspectral imaging: A case study with Tethysphytum antarcticum (Ross Sea, Antarctica). Journal of Phycology 60, 695–709. URL: https://onlinelibrary.wiley.com/doi/abs/10.1111/jpy.13449, doi:10.1111/jpy.13449. _eprint: https://onlinelibrary.wiley.com/doi/pdf/10.1111/jpy.13449.

Montes-Herrera, J.C., Robbins, A., Franson, C., Bektas, T., Sparrow, B., Lucieer, A., 2025. DroneScape: Collection of Penta-Return LiDAR for Ecosystem Plot Monitoring URL: https://www.protocols.io/print/dronescape-collection-of-penta-return-lidar-for-ec-g3c3byiyp.

Morgan, B.E., Chipman, J.W., Bolger, D.T., Dietrich, J.T., 2020. Spatiotemporal Analysis of Vegetation Cover Change in a Large Ephemeral River: Multi-Sensor Fusion of Unmanned Aerial Vehicle (UAV) and Landsat Imagery. Remote Sensing 13, 51. URL: https://www.mdpi.com/2072-4292/13/1/51, doi:10.3390/rs13010051.

Mosig, C., Vajna-Jehle, J., Mahecha, M.D., Cheng, Y., Hartmann, H., Montero, D., Junttila, S., Horion, S., Schwenke, M.B., Koontz, M.J., Maulud, K.N.A., Adu-Bredu, S., Al-Halbouni, D., Ali, M., Allen, M., Altman, J., Amorós, L., Angiolini, C., Astrup, R., Awada, H., Barrasso, C., Bartholomeus, H., Beck, P.S.A., Bozzini, A., Braun-Wimmer, J., Brede, B., Breunig, F.M., Brugnaro, S., Buras, A., Burchard-Levine, V., Camarero, J.J., Candotti, A., Capuder, L., Carrieri, E., Centritto, M., Chirici, G., Cloutier, M., Conciani, D., Cushman, K., Dalling, J.W., Dao, P.D., Dempewolf, J., Denter, M., Dogotari, M., Díaz-Delgado, R., Ecke, S., Eichel, J., Eltner, A., Fabbri, A., Fabi, M., Fassnacht, F., Ferreira, M.P., Fischer, F.J., Frey, J., Frick, A., Fuentes, J., Ganz, S., Garbarino, M., García, M., Gassilloud, M., Gazol, A., Gea-Izquierdo, G., Gerberding, K., Ghasemi, M., Giannetti, F., Gillan, J., Gonzalez, R., Gosper, C., Greene, T., Greinwald, K., Grieve, S., Große-Stoltenberg, A., Gutierrez, J.A., Göritz, A., Hajek, P., Hedding, D., Hempel, J., Heremans, S., Hernández, M., Heurich, M., Honkavaara, E., Höfle, B., Jackisch, R., Jucker, T., Kalwij, J.M., Kepfer-Rojas, S., Khatri-Chhetri, P., Kleinebecker, T., Klemmt, H.J., Klouček, T., Koivumäki, N., Kolagani, N., Komárek, J., Korznikov, K., Kraszewski, B., Kruse, S., Krüger, R.,

Kuechly, H., Kwong, I.H.Y., Laliberté, E., Langan, L., Latifi, H., Leal-Medina, C., Lehmann, J.R.K., Li, L., Lines, E., Lisiewicz, M., Lopatin, J., Lucieer, A., Ludwig, A., Ludwig, M., Lyytikäinen-Saarenmaa, P., Ma, Q., Mansuy, N., Peña, J.M., Marino, G., Maroschek, M., Martín, M.P., Martín-Benito, D., Matham, P., Mazzoni, S., Meloni, F., Menzel, A., Meyer, H., Miraki, M., Moreno, G., Moreno-Fernández, D., Muller-Landau, H.C., Mälicke, M., Möhring, J., Müllerova, J., Naidu, S.S., Nardi, D., Neumeier, P., Nita, M.D., Näsi, R., Oppgenoorth, L., Orunbaev, S., Palmer, M., Paul, T., Pfenning, M., Potts, A., Prasanna, G.L., Prober, S., Puliti, S., Pérez-Luque, A.J., Pérez-Priego, O., Reudenbach, C., Revuelto, J., Rivas-Torres, G., Roberge, P., Roggero, P.P., Rossi, C., Ruehr, N.K., Ruiz-Benito, P., Runge, C.M., Satta, G.G.A., Scanu, B., Scherer-Lorenzen, M., Schiefer, F., Schiller, C., Schladebach, J., Schmehl, M.T., Schmid, J., Schmidt, T.A., Schwarz, S., Seidl, R., Seifert, T., Barba, A.S., Shafeian, E., Shapiro, A., de Simone, L., Sohrabi, H., Soltani, S., Sotomayor, L., Sparrow, B., Steer, B.S.C., Stenson, M., Stöckigt, B., Su, Y., Suomalainen, J., Tamudo, E., Barbieri, M.J.T., Tomelleri, E., Torresani, M., Trepekli, K., Ullah, S., Ullah, S., Umlauft, J., Vargas-Ramírez, N., Vatandaslar, C., Visacki, V., Volpi, M., Vásquez, V., Wallis, C., Weinstein, B., Weiser, H., Wich, S., Ximena, T.C., Zarco-Tejada, P.J., Zdunic, K., Zielewska-Büttner, K., de Oliveira, R.A., van Wagtendonk, L., von Dosky, V., Kattenborn, T., 2026. deadtrees.earth — An open-access and interactive database for centimeter-scale aerial imagery to uncover global tree mortality dynamics. Remote Sensing of Environment 332, 115027. URL: https://www.sciencedirect.com/science/article/pii/S0034425725004316, doi:10.1016/j.rse.2025.115027.

Möhring, J., Kattenborn, T., Mahecha, M.D., Cheng, Y., Beloiu Schwenke, M., Cloutier, M., Denter, M., Frey, J., Gassilloud, M., Göritz, A., Hempel, J., Horion, S., Jucker, T., Junttila, S., Khatri-Chhetri, P., Korznikov, K., Kruse, S., Laliberté, E., Maroschek, M., Neumeier, P., Pérez-Priego, O., Potts, A., Schiefer, F., Seidl, R., Vajna-Jehle, J., Zielewska-Büttner, K., Mosig, C., 2025. Global, multi-scale standing deadwood segmentation in centimeter-scale aerial images. ISPRS Open Journal of Photogrammetry and Remote Sensing 18, 100104. URL: https://www.sciencedirect.com/science/article/pii/S2667393225000237, doi:10.1016/j.ophoto.2025.100104.

Reddig, F., Hütt, C., Jenal, A., Wolf, J., Bareth, G., 2025. The Invisible Plant: Estimating Fractional Vegetation Cover of Tillandsia landbeckii in the Atacama Desert using Hyperspectral EnMAP and High-Resolution Validation Data. PFG – Journal of Photogrammetry, Remote Sensing and Geoinformation Science 93, 583–609. URL: https://doi.org/10.1007/s41064-025-00358-7, doi:10.1007/s41064-025-00358-7.

RESE, 2025. Droacor - Rese Remote Sensing Software. URL: https://www.rese-apps.com/droacor/.

Ronneberger, O., Fischer, P., Brox, T., 2015. U-Net: Convolutional Networks for Biomedical Image Segmentation, in: Navab, N., Hornegger, J., Wells, W.M., Frangi, A.F. (Eds.), Medical Image Computing and Computer-Assisted Intervention – MICCAI 2015, Springer International Publishing, Cham. pp. 234–241. doi:10.1007/978-3-319-24574-4_28.

Růžička, V., Markham, A., 2024. HyperspectralViTs: General Hyperspectral Models for On-board Remote Sensing. URL: https://arxiv.org/abs/2410.17248v3, doi:10.1109/JSTARS.2025.3557527.

Sandino, J., Barthelemy, J., Doshi, A., Randall, K., Robinson, S.A., Bollard, B., Gonzalez, F., 2025. Drone hyperspectral imaging and artificial intelligence for monitoring moss and lichen in Antarctica. Scientific Reports 15, 27244. URL: https://www.nature.com/articles/s41598-025-11535-4, doi:10.1038/s41598-025-11535-4. tex.copyright: 2025 The Author(s).

Scheiter, M., Valentine, A., Sambridge, M., 2022. Upscaling and downscaling Monte Carlo ensembles with generative models. Geophysical Journal International 230, 916–931. URL: https://doi.org/10.1093/gji/ggac100, doi:10.1093/gji/ggac100.

Schiefer, F., Kattenborn, T., Frick, A., Frey, J., Schall, P., Koch, B., Schmidtlein, S., 2020. Mapping forest tree species in high resolution UAV-based RGB-imagery by means of convolutional neural networks. ISPRS Journal of Photogrammetry and Remote Sensing 170, 205–215. URL: https://www.sciencedirect.com/science/article/pii/S0924271620302938, doi:10.1016/j.isprsjprs.2020.10.015.

Schiefer, F., Schmidtlein, S., Frick, A., Frey, J., Klinke, R., Zielewska-Büttner, K., Junttila, S., Uhl, A., Kattenborn, T., 2023. UAV-based reference data for the prediction of fractional cover of standing deadwood from Sentinel time series. ISPRS Open Journal of Photogrammetry and Remote Sensing 8, 100034. URL: https://www.sciencedirect.com/science/article/pii/S2667393223000054, doi:10.1016/j.ophoto.2023.100034.

Sothe, C., , C. M., D.A., , M. B., S., , L. E. C., L.R., , J. D. B., C., , R. Q., F., , M., D., , C. L., L., , V., L., , G. T., M., , Tommaselli, A.M.G., 2020. Comparative performance of convolutional neural network, weighted and conventional support vector machine and random forest for classifying tree species using hyperspectral and photogrammetric data. GIScience & Remote Sensing 57, 369–394. URL: https://doi.org/10.1080/15481603.2020.1712102, doi:10.1080/15481603.2020.1712102.

Sotomayor, L.N., Lucieer, A., Turner, D., Barthelemy, J., Kattenborn, T., 2026. From 2D labels to 3D structure: Scalable label transfer and benchmarking of 3D vegetation models in rangeland ecosystems URL: https://eartharxiv.org/repository/view/12889/. tex.copyright: CC BY Attribution 4.0 International.

Sotomayor, L.N., Lucieer, A., Turner, D., Lewis, M., Kattenborn, T., 2025a. Mapping fractional vegetation cover in UAS RGB and multispectral imagery in semi-arid Australian ecosystems using CNN-based semantic segmentation. Landscape Ecology 40, 169. URL: https://doi.org/10.1007/s10980-025-02193-y, doi:10.1007/s10980-025-02193-y.

Sotomayor, L.N., Megan, L., Krishna, L., Hoyer, S., Molly, M., Arko, L., 2025b. Fractional Vegetation Cover Mapping - UAS RGB and Multispectral Imagery, CNN algorithms, Semi-Arid Australian Ecosystems Coverage URL: https://zenodo.org/records/15036860.

Sotomayor, L.N., Megan, L., Krishna, L., Sophia, H., Molly, M., Arko, L., 2025c. Fractional vegetation cover mapping - UAS RGB and multispectral imagery, CNN algorithms, semi-arid australian ecosystems coverage. URL: https://doi.org/10.5281/zenodo.15036860, doi:10.5281/zenodo.15036860.

Storch, T., Honold, H.P., Chabrillat, S., Habermeyer, M., Tucker, P., Brell, M., Ohndorf, A., Wirth, K., Betz, M., Kuchler, M., Mühle, H., Carmona, E., Baur, S., Mücke, M., Löw, S., Schulze, D., Zimmermann, S., Lenzen, C., Wiesner, S., Aida, S., Kahle, R., Willburger, P., Hartung, S., Dietrich, D., Plesia, N., Tegler, M., Schork, K., Alonso, K., Marshall, D., Gerasch, B., Schwind, P., Pato, M., Schneider, M., de los Reyes, R., Langheinrich, M., Wenzel, J., Bachmann, M., Holzwarth, S., Pinnel, N., Guanter, L., Segl, K., Scheffler, D., Foerster, S., Bohn, N., Bracher, A., Soppa, M.A., Gascon, F., Green, R., Kokaly, R., Moreno, J., Ong, C., Sornig, M., Wernitz, R., Bagschik, K., Reintsema, D., La Porta, L., Schickling, A., Fischer, S., 2023. The EnMAP imaging spectroscopy mission towards operations. Remote Sensing of Environment 294, 113632. URL: https://www.sciencedirect.com/science/article/pii/S0034425723001839, doi:10.1016/j.rse.2023.113632.

TERN, 2021. Summary of TERN plots on Calperum, South Australia.

TERN, L., 2022. Field Survey Apps & Protocols | TERN Land Ecosystem Research Network. URL: https://www.tern.org.au/field-survey-protocols/.

TERN, L., Monitoring, T.S., Stenson, M., Sparrow, B., Lucieer, A., 2022. Drone RGB and Multispectral Imagery from TERN plots across Australia. URL: https://portal.tern.org.au/metadata/TERN/39de90f5-49e3-4567-917c-cf3e3bc93086.

TERN, T.E.R.N., 2026. terndata.ecoplots 1.0.0 documentation. URL: https://terndata-ecoplots.readthedocs.io/en/latest/.

Tucker, C.J., 1979. Red and photographic infrared linear combinations for monitoring vegetation. Remote Sensing of Environment 8, 127–150. URL: https://www.sciencedirect.com/science/article/pii/0034425779900130, doi:10.1016/0034-4257(79)90013-0.

Turner, D., Cimoli, E., Lucieer, A., Haynes, R.S., Randall, K., Waterman, M.J., Lucieer, V., Robinson, S.A., 2023. Mapping water content in drying Antarctic moss communities using UAS-borne SWIR imaging spectroscopy. Remote Sensing in Ecology and Conservation n/a. URL: https://onlinelibrary.wiley.com/doi/abs/10.1002/rse2.371, doi:10.1002/rse2.371. tex.copyright: © 2023 The Authors.

Remote Sensing in Ecology and Conservation published by John Wiley & Sons Ltd on behalf of Zoological Society of London.

Turner, D., Cimoli, E., Lucieer, A., Haynes, R.S., Randall, K., Waterman, M.J., Lucieer, V., Robinson, S.A., 2024. Mapping water content in drying Antarctic moss communities using UAS-borne SWIR imaging spectroscopy. Remote Sensing in Ecology and Conservation 10, 296–311. URL: https://onlinelibrary.wiley.com/doi/abs/10.1002/rse2.371, doi:10.1002/rse2.371. tex.copyright: © 2023 The Authors. Remote Sensing in Ecology and Conservation published by John Wiley & Sons Ltd on behalf of Zoological Society of London.

Ustin, S.L., Gamon, J.A., 2010. Remote sensing of plant functional types. New Phytologist 186, 795–816. URL: https://onlinelibrary.wiley.com/doi/abs/10.1111/j.1469-8137.2010.03284.x, doi:10.1111/j.1469-8137.2010.03284.x. _eprint: https://nph.onlinelibrary.wiley.com/doi/pdf/10.1111/j.1469-8137.2010.03284.x.

Vaswani, A., Shazeer, N., Parmar, N., Uszkoreit, J., Jones, L., Gomez, A.N., Kaiser, L., Polosukhin, I., 2023. Attention Is All You Need. URL: http://arxiv.org/abs/1706.03762, doi:10.48550/arXiv.1706.03762. arXiv:1706.03762 [cs.CL].

Veitch-Michaelis, J., Cottam, A., Schweizer, D., Broadbent, E.N., Dao, D., Zhang, C., Zambrano, A.A., Max, S., 2024. OAM-TCD: A globally diverse dataset of high-resolution tree cover maps. URL: http://arxiv.org/abs/2407.11743, doi:10.48550/arXiv.2407.11743. arXiv:2407.11743 [cs.CV].

Wada, K., others, 2021. wkentaro/labelme: v4.6.0. URL: https://zenodo.org/records/5711226, doi:10.5281/zenodo.5711226.

Wang, X., Liu, S., Shen, X., Shen, C., Jia, J., 2019a. Associatively Segmenting Instances and Semantics in Point Clouds. URL: http://arxiv.org/abs/1902.09852, doi:10.48550/arXiv.1902.09852.

Wang, Z., Townsend, P.A., Schweiger, A.K., Couture, J.J., Singh, A., Hobbie, S.E., Cavender-Bares, J., 2019b. Mapping foliar functional traits and their uncertainties across three years in a grassland experiment. Remote Sensing of Environment 221, 405–416. URL: https://www.sciencedirect.com/

science/article/pii/S003442571830525X, doi:10.1016/j.rse.2018.11.016.

White, A., Sparrow, B., Leitch, E., Foulkes, J., Flitton, R., Lowe, A.J., Caddy-Retalic, S., 2012. AusPlots Rangelands Survey Protocols Manual. University of Adelaide Press. URL: https://digital.library.adelaide.edu.au/dspace/handle/2440/101955. tex.copyright: © The Authors 2012 This book is copyright. Apart from any fair dealing for the purposes of private study, research, criticism or review as permitted under the Copyright Act, no part may be reproduced, stored in a retrieval system, or transmitted, in any form or by any means, electronic, mechanical, photocopying, recording or otherwise without the prior written permission.

Xie, E., Wang, W., Yu, Z., Anandkumar, A., Alvarez, J.M., Luo, P., 2021. SegFormer: Simple and Efficient Design for Semantic Segmentation with Transformers. URL: http://arxiv.org/abs/2105.15203, doi:10.48550/arXiv.2105.15203. arXiv:2105.15203 [cs.CV].

Xiong, Y., Varadarajan, B., Wu, L., Xiang, X., Xiao, F., Zhu, C., Dai, X., Wang, D., Sun, F., Iandola, F., Krishnamoorthi, R., Chandra, V., 2023. EfficientSAM: Leveraged Masked Image Pretraining for Efficient Segment Anything. URL: http://arxiv.org/abs/2312.00863, doi:10.48550/arXiv.2312.00863.

Xiong, Y., Zhou, C., Xiang, X., Wu, L., Zhu, C., Liu, Z., Suri, S., Varadarajan, B., Akula, R., Iandola, F., Krishnamoorthi, R., Soran, B., Chandra, V., 2024. Efficient Track Anything. URL: http://arxiv.org/abs/2411.18933, doi:10.48550/arXiv.2411.18933.

Xue, J., Su, B., 2017. Significant Remote Sensing Vegetation Indices: A Review of Developments and Applications. Journal of Sensors 2017, 1353691. URL: https://onlinelibrary.wiley.com/doi/abs/10.1155/2017/1353691, doi:10.1155/2017/1353691. tex.copyright: Copyright © 2017 Jinru Xue and Baofeng Su.

Yang, D., Morrison, B.D., Hantson, W., Breen, A.L., McMahon, A., Li, Q., Salmon, V.G., Hayes, D.J., Serbin, S.P., 2021. Landscape-scale characterization of Arctic tundra vegetation composition, structure, and function with a multi-sensor unoccupied aerial system. Environmental Re-

search Letters 16, 085005. URL: https://doi.org/10.1088/1748-9326/ac1291, doi:10.1088/1748-9326/ac1291. publisher: IOP Publishing.

Zhao, Y., Sun, Y., Lu, X., Zhao, X., Yang, L., Sun, Z., Bai, Y., 2021. Hyperspectral retrieval of leaf physiological traits and their links to ecosystem productivity in grassland monocultures. Ecological Indicators 122, 107267. URL: https://www.sciencedirect.com/science/article/pii/S1470160X20312073, doi:10.1016/j.ecolind.2020.107267.

References

Leslie Lamport, *LaTeX: a document preparation system*, Addison Wesley, Massachusetts, 2nd edition, 1994.